J. Fluid Mech. (1991), *vol.* 232, *pp.* 133–165
Printed in Great Britain

Vortex-induced boundary-layer separation. Part 2. Unsteady interacting boundary-layer theory

By VALLORIE J. PERIDIER,[1] F. T. SMITH[2] AND J. D. A. WALKER[3]

[1] Department of Mechanical Engineering, Temple University, Philadelphia, PA 19122, USA

[2] Department of Mathematics, University College London, Gower Street, London WC1E 6BT, UK

[3] Department of Mechanical Engineering and Mechanics, Lehigh University, Bethlehem, PA 18015, USA

(Received 28 September 1990 and in revised form 23 April 1991)

The unsteady boundary layer induced by the motion of a rectilinear vortex above an infinite plane wall is calculated using interacting boundary-layer methods. The boundary-layer solution is computed in Lagrangian variables since it is possible to compute the flow evolution accurately in this formulation even when an eruption starts to evolve. Results are obtained over a range of Reynolds numbers, Re. For the limit problem $Re \to \infty$ (studied in Part 1), a singularity develops in the non-interacting boundary-layer solution at finite time. The present results show that the interacting boundary-layer calculations also terminate in a singularity at a time which is earlier than in the limit problem and which decreases with decreasing Reynolds number. The computed results are compared with the length- and timescales predicted by recent asymptotic theories and are found to be in excellent agreement.

1. Introduction

This study is the second part of an investigation into the viscous response induced near a solid wall by the motion of a vortex above the surface when the flow is at high Reynolds number. A principal motivation of this work is to understand the basic physical mechanisms of turbulence production and regeneration near a solid surface, as described in Part 1 (Peridier, Smith & Walker 1991). It is widely believed (see, for example, Head & Bandyopadhyay 1981; Perry & Chong 1982; Acarlar & Smith 1987*a*, *b*; Walker *et al.* 1989; Smith *et al.* 1990; Walker 1990*a*, *b*) that the convected hairpin vortex is a central element in the structure of the turbulent boundary layer and, further, that the moving vortex provokes a discrete eruption of the turbulent wall layer whenever such a vortex is in the proximity of the surface for a sufficient period of time (Walker 1990*a*, *b*; Smith *et al.* 1991). In this study, a model problem is considered corresponding to a rectilinear vortex in motion above an infinite plane wall in an otherwise stagnant fluid. This configuration is addressed because it represents the simplest type of vortex-induced boundary-layer eruption and the general nature of the subsequent interaction with the external flow is reasonably well-documented from experiments (Harvey & Perry 1971; Walker *et al.* 1987; Chu & Falco 1988).

If κ denotes the vortex strength and ν is the kinematic viscosity, a Reynolds number for the problem may be defined by $Re = \kappa/(2\nu)$. In Part 1 of this study the

evolution of the boundary-layer flow for the limit problem $Re \to \infty$ was considered. It was demonstrated that flow near the surface focuses abruptly into an erupting spike and that a singularity evolves at finite time. Furthermore, the terminal singularity structure is the same as that found by Van Dommelen & Shen (1980) for the impulsively started circular cylinder and corresponds to what Van Dommelen (1981) has referred to as 'upstream-slipping separation'. The terminal singularity is also discussed by Elliott, Cowley & Smith (1983), who point out that it may be a generic state for many unsteady two-dimensional flows. The dynamics of the phenomenon are such that once the boundary layer starts to focus into an eruptive spike, the equations governing the local processes become independent of the external pressure gradient that originally initiated the phenomenon. This view is supported by extensive numerical work on a variety of unsteady two-dimensional boundary-layer problems (see, for example, Doligalski & Walker 1984; Ece, Walker & Doligalski 1984; Ersoy & Walker 1985, 1986) which ultimately terminate in the abrupt evolution of a spike in the displacement thickness.

In a limit analysis ($Re \to \infty$), the pressure distribution is computed from an inviscid solution and is assumed prescribed for the boundary-layer flow. If the flow is initiated impulsively, for example, the flow field starts out as double-structured with an outer inviscid region and a thin boundary layer; in these circumstances a classical non-interactive calculation method is appropriate, at least initially. However, as soon as strong boundary-layer growth develops, it is necessary to account for an interaction with the external inviscid flow. Effectively, a singularity develops in the unsteady boundary-layer solution in the limit problem $Re \to \infty$ (Part 1) because of the attempt to treat the pressure gradient as prescribed for an indefinite period of time. The evolution of a singularity thus tends to be indicative of the need to develop an interactive strategy, and there are at least two ways in which this may be carried out. The first of these is to continue consideration of the limit problem $Re \to \infty$ and to determine the Reynolds-number dependence of the length- and timescales that develop locally as the boundary-layer solution breaks down, with the onset of an eruption of the surface flow. The second alternative is to develop an interacting boundary-layer (IBL) approach in which a finite but large value of the Reynolds number is adopted and the influence of the thickening boundary layer is accounted for.

Consider first a continuation of a limit analysis. Van Dommelen & Shen (1982) and Elliott *et al.* (1983) have described the singularity which is the terminal state of the classical boundary-layer solution. As the singularity forms (see, for example, Van Dommelen & Shen 1980; Part 1), the displacement thickness develops a sharp spike locally as the flow proceeds toward a narrow, focused boundary-layer eruption (see, for example, figure 4 of Part 1). The boundary layer bifurcates into three regions consisting of two passive shear layers, one near the surface and one moving rapidly away from the wall; sandwiched in between there is an explosively growing intermediate region where the dynamics are primarily nonlinear and inviscid (see figure 5*a* of Part 1). The singularity generally forms off the wall at some position along a zero-vorticity line, whose presence at some earlier time within the boundary-layer flow is a necessary condition for an eruption to subsequently occur. Assume that the singularity in the boundary-layer solution occurs at time t_s and a streamwise location x_s. At the time of formation, the singularity is moving in most cases and we assume what is apparently the most common situation where the motion is upstream relative to the local inviscid flow. Using the terminology of Van Dommelen & Shen (1982), this situation is referred to as 'upstream-slipping separation'; in the notation

of Elliott *et al.* (1983), the velocity of the singularity is $-K$, with $K > 0$. An important aspect of the terminal singular structure is that it is independent of the local mainstream pressure gradient. Consequently, a wide variety of external pressure fields can lead to the evolution of a zero-vorticity line within the boundary layer and a subsequent focusing of the flow toward an eruption. However, the flow near the eruption rapidly 'forgets' the pressure distribution which initiated the process, and the clear suggestion of the work of Elliott *et al.* (1983) is that the terminal singularity structure is a generic state reached by most two-dimensional erupting boundary layers.

An important question relates to how the singularity is relieved and Elliott *et al.* (1983) argue that the pressure gradient in the mainstream induced by the explosively growing displacement-thickness spike starts to influence the boundary-layer solution in the intermediate region (within the spike) when $t_s - t$ is $O(Re^{-\frac{3}{11}})$. This stage of development will be referred to here as the first interactive stage, for which Elliott *et al.* (1983) define the following scaled variables:

$$(x-x_s)-K(t_s-t) = Re^{-\frac{3}{11}}X_I, \quad Y = Re^{-\frac{5}{11}}Y_I, \quad t-t_s = Re^{-\frac{3}{11}}t_I, \tag{1}$$

with dependent variables

$$u = -K+Re^{-\frac{1}{11}}U_I(X_I, Y_I, t_I), \quad p = Re^{-\frac{2}{11}}P_I(X_I, Y_I, t_I). \tag{2}$$

Here (x, Y) are dimensionless Cartesian coordinates with corresponding velocity components (u, v) and p is the pressure. A schematic diagram of this first interactive stage is given in figure 1. Region I is a passive region near the wall while region III is a passive shear layer which is moving rapidly away from the wall with position described by $Y_I = \beta_I(X_I, t_I)$. To match to the terminal boundary-layer structure described in §7 of Part 1, it can be shown that the required initial condition for the first interactive stage is $\beta_I \sim 2\tilde{Y}_0(\tilde{X})(-t_I)^{-\frac{1}{4}}$ as $t_I \to -\infty$. Equations (1) and (2) define variables in the central region II where the governing equations are

$$\frac{\partial U_I}{\partial t_I}+U_I\frac{\partial U_I}{\partial X_I}-\frac{\partial \psi_I}{\partial X_I}\frac{\partial U_I}{\partial Y_I} = -\frac{\partial P_I}{\partial X_I}, \quad U_I = \frac{\partial \psi_I}{\partial Y_I}. \tag{3}$$

The matching to the upper and lower passive layers requires (for the symmetric structure assumed by Elliott *et al.* 1983; see Part 1) that

$$U_I \sim \frac{4}{Y_I^2} \quad \text{as} \quad Y_I \to 0; \qquad U_I \sim \frac{4}{(Y_I-\beta_I)^2} \quad \text{as} \quad Y_I \to \beta_I. \tag{4}$$

The growth of region II provokes a local response in the inviscid flow in region IV and leads to the following pressure-displacement relation:

$$P_I = \frac{1}{\pi}\int_{-\infty}^{\infty}\frac{\partial \beta_I}{\partial \xi}\frac{d\xi}{X_I-\xi}, \tag{5}$$

where the right-hand side of (5) is a Cauchy principal value integral. The unusual boundary conditions in (4) pose computational difficulties, and to date attempts to produce numerical solutions for this first interactive stage have been unsuccessful. However, it seems likely that this stage will also terminate in a singularity and that it may be necessary to go through a number of complex interactive stages with increasingly shorter timescales before the erupting boundary-layer fluid penetrates a

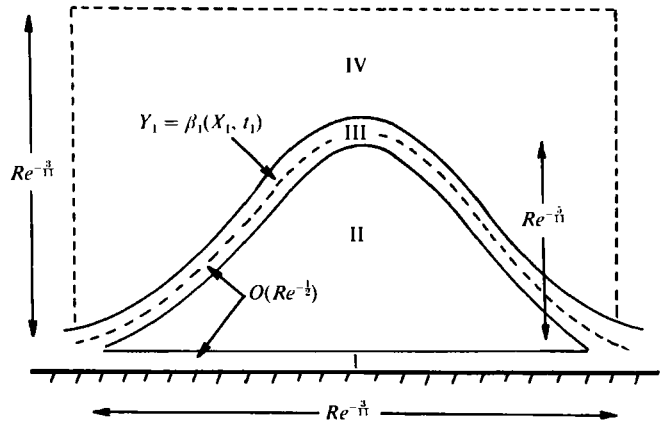

FIGURE 1. Schematic diagram (not to scale) of the first interactive stage.

distance $O(1)$ away from the wall. In view of the apparent complexity of the limit analysis, the second alternative of interacting boundary-layer (IBL) theory appears worth pursuing.

The IBL approach for *steady* flows has been well developed in recent times. It is well known (see, for example, Stewartson 1974; Smith 1982) that the IBL methodology, when properly applied, relieves the Goldstein (1948) singularity that is known to occur in the solution of the steady boundary-layer equations when the mainstream pressure gradient is adverse and prescribed. Although Elliott *et al.* (1983) have shown that the unsteady separation singularity is not of the Goldstein type (as proposed by Sears & Telionis 1971, 1975), there has been interest in recent times in using an unsteady IBL approach to try to relieve the singularity and carry the boundary-layer computations on further in time. The basis of the conventional IBL methodology is to assume that perturbations induced by the boundary layer on the external flow field are small and this leads to a Cauchy principal value integro-differential equation relating the mainstream pressure to the displacement thickness. It is clearly evident, from a variety of experimental studies on vortex-induced separation (see, for example, Harvey & Perry 1971; Walker *et al.* 1987), that the IBL approach can be valid for only a limited period of time since the observed viscous–inviscid interactions are strong and involve $O(1)$ changes in the external flow field. Nevertheless, the approach is worth pursuing and has been considered for: (i) the impulsively started circular cylinder by Henkes & Veldman (1987) and Riley & Vasantha (1989); (ii) vortex-induced separation by Chuang & Conlisk (1980), Conlisk (1989) and Riley & Vasantha (1989); and (iii) the boundary layer on a pitching airfoil by Cebeci, Khattab & Schimke (1988). The results of these studies have been somewhat inconclusive. Henkes & Veldman (1987) and Riley & Vasantha (1989) tentatively conclude that the IBL approach may postpone or perhaps relieve the separation singularity. On the other hand, the IBL calculations of Chuang & Conlisk (1989) could not be continued beyond a certain time, and they indicated that this may be due to the onset of a singularity. The pitching airfoil computations of Cebeci *et al.* (1988) were also terminated at a finite time for reasons which were not explained.

Some of the cited computational experience with unsteady IBL calculations seem currently at variance with a theoretical investigation of Smith (1988*a*), who concluded that a singularity can occur at finite time in any unsteady IBL

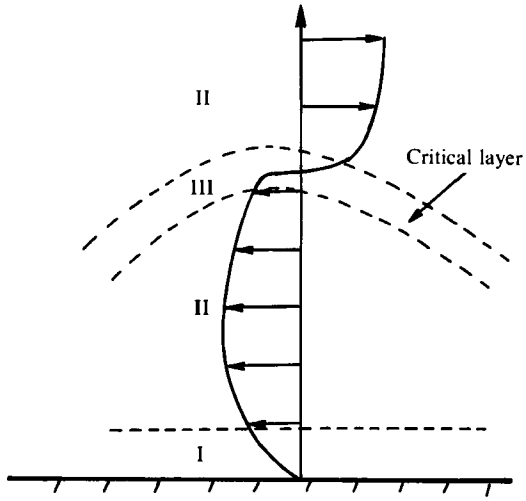

FIGURE 2. Schematic of the three-zone region, with typical velocity profile, for the interactive singularity structure.

formulation (see also Brown, Cheng & Smith 1988; Brotherton-Ratcliffe & Smith 1987). A brief description of the main features of Smith's (1988*a*) asymptotic solution will be given here in order to facilitate later comparison with the results of this study. Assume that a singularity can occur at time t_s and at $x = x_s$ and consider a thinning zone which is moving toward x_s with speed C (where C is to be found); the streamwise scaling adopted by Smith (1988*a*) is

$$\xi' = (x - x_s + CT)\, T^{-\frac{3}{2}}, \quad T = t_s - t. \tag{6}$$

Smith (1988*a*) argues that the boundary layer splits into three zones as $t \to t_s-$ which are shown schematically in figure 2. If $y = Re^{\frac{1}{2}}\, Y$ denotes the scaled boundary-layer variable, then the main zone (zone II) is inviscid and has $y = O(1)$; here the velocity profile $U_0(y)$ is generally rotational and is shown in figure 2 with an arbitrary shape. The streamwise velocity in region II is expanded in the form

$$u = U_0(y) + T^{\frac{1}{2}} U_1(\xi', y) + T^{\frac{3}{4}} U_2(\xi', y) + T U_3(\xi', y) + \ldots, \tag{7}$$

where $U_0(y)$ is the (arbitrary) velocity profile at $x = x_0$ as $t \to t_s$. The profile functions U_i, $i = 1, 2, \ldots$ are determined from inviscid equations, and a viscous wall layer (region I) is required in order to reduce these functions to relative rest on the surface; the solution in region I depends on ξ' and the scaled variable $\tilde{\eta} = T^{-\frac{3}{4}} y$. The third zone in figure 2 is a critical layer across which the profile function U_3 in (7) exhibits a jump in velocity. The critical layer is mainly inviscid and nonlinear. Smith (1988*a*) has obtained detailed solutions for zone III and from this determines that the pressure develops irregular behaviour as $t \to t_s$ with

$$p - p_0 = O((x - x_s)^{\frac{1}{3}}) \quad \text{as} \quad x \to x_s \pm, \tag{8}$$

where p_0 is a constant. The pressure gradient is therefore singular as $t \to t_s$ and the theory predicts that the maximum values of the pressure gradient and normal velocity are of the form

$$\left.\frac{\mathrm{d}p}{\mathrm{d}x}\right|_{\max} \sim \frac{C_1}{t_s - t}, \quad v_{\max} \sim \frac{C_2}{t_s - t}, \tag{9}$$

where C_1 and C_2 are constants. The shear-stress distribution on the surface is also predicted to develop a singularity with a local maximum behaving according to

$$\tau_{w_{max}} \sim \frac{C_3}{(t_s - t)^{\frac{1}{4}}}, \tag{10}$$

where C_3 is a constant.

In the present study, interacting boundary-layer solutions were obtained for the model problem described in Part 1 (see also §2 below) over a range of Reynolds numbers (10^5–10^8). All previous IBL calculations cited above were carried out using a conventional Eulerian method to compute the boundary-layer flow and encountered severe difficulty in accurately evaluating the intense variations that develop as the surface flow starts to focus into an eruption. The present results are the first IBL solutions obtained using a Lagrangian algorithm for the boundary layer; this permits computation well beyond the times at which an Eulerian scheme would typically fail, and in any case enables numerical integrations to be carried out all the way through to the formation of a singularity. The use of Lagrangian schemes and their clear advantages over Eulerian formulations have been reviewed recently by Cowley, Van Dommelen & Lam (1990) in the non-interactive context. It is found in the present work that rather than delay the onset of singular behaviour, the effect of interaction is to promote boundary-layer breakdown at an *earlier* time. The present results confirm the scalings obtained by Elliott *et al.* (1983) for the first interactive stage and, although the unsteady separation singularity appears to be relieved through the IBL approach, a second singularity quickly occurs. Furthermore, the present results appear to confirm quantitatively that this second singularity is that described by Smith (1988*a*) in what was termed 'moderate break-up' of the interacting boundary-layer formulation.

2. Interactive equations

Consider a rectilinear vortex of strength κ which is placed in an otherwise stagnant flow above an infinite plane at a distance a from the wall at time $t = 0$. As discussed in Part 1, inviscid theory predicts that such a vortex will remain at constant height a from the wall and be convected to the right in the velocity field of its image with speed $V_c = \kappa/2a$ (Walker 1978). Upon the initiation of this motion, a thin unsteady boundary layer develops along the wall. The boundary-layer thickness is initially $O(Re^{-\frac{1}{8}})$, where the Reynolds number may be defined by

$$Re = \frac{aV_c}{\nu} = \frac{\kappa}{2\nu}, \tag{11}$$

and ν is the kinematic viscosity. To define dimensionless variables, it is convenient to adopt a and V_c as a representative length and velocity, respectively, corresponding to distance from the wall and vortex speed at $t = 0$. Let (x, Y) denote Cartesian coordinates measuring distance tangential and normal to the surface respectively, with corresponding velocity components (u, V). In the boundary layer, the scaled variables

$$y = Re^{\frac{1}{8}}Y, \quad v = Re^{\frac{1}{8}}V \tag{12}$$

are utilized and the velocity components are (u, v). Let $(X_v(t), Y_v(t))$ denote the position of the vortex at time t relative to the wall and let $(U_v(t), V_v(t))$ be the velocity of the vortex. In the limit problem $Re \to \infty$, previously considered in Part 1, the vortex

trajectory is determined from the leading-order inviscid solution, for which the sole influence on the vortex is the image vortex below the plate. It was shown that

$$Y_v = 1, \quad U_v = 1, \quad V_v = 0 \quad (Re \to \infty), \tag{13}$$

and X_v increases linearly with t. In the present study, large but finite values of Re are considered using interacting boundary layer (IBL) concepts. In the IBL approach, the influence of the boundary layer is assumed small but is nevertheless accounted for through an interaction condition. In the following development, a quasi-steady interactive formulation will be given.

Consider a general boundary-layer flow described by a stream function ψ defined by

$$u = \frac{\partial \psi}{\partial y}, \quad v = -\frac{\partial \psi}{\partial x}. \tag{14}$$

Matching of the boundary layer to the external mainstream requires

$$u \to U_e(x,t) \quad \text{as} \quad y \to \infty, \tag{15}$$

and it is easily verified that

$$\psi \sim U_e(x,t)\{y - \delta^*(x,t)\} \quad \text{as} \quad y \to \infty, \tag{16}$$

where

$$\delta^* = \int_0^\infty \left\{1 - \frac{u(x,y,t)}{U_e(x,t)}\right\} dy \tag{17}$$

is the displacement thickness. Using (12), it can be verified that the external velocity distribution must have

$$V \sim -\frac{\partial U_e}{\partial x} Y + Re^{-\frac{1}{2}} V_d(x,t) + \ldots \quad \text{as} \quad Y \to 0, \tag{18}$$

in order to match the boundary-layer solution. Here V_d is the scaled displacement velocity induced near the surface by the boundary-layer flow and

$$V_d(x,t) = \frac{\partial}{\partial x}\left\{U_e(x,t)\,\delta^*(x,t)\right\}. \tag{19}$$

It is evident from (18) that the form of solution in the inviscid region is

$$(u, V) = (U_0, V_0) + Re^{-\frac{1}{2}}(U_1, V_1) + \ldots, \tag{20}$$

to first order. Here (U_0, V_0) is the leading-order inviscid solution, normally utilized in a non-interacting calculation procedure, while (U_1, V_1) are velocities associated with a perturbation $O(Re^{-\frac{1}{2}})$. A perturbation stream function Ψ_1 may be defined by

$$U_1 = \frac{\partial \Psi_1}{\partial Y}, \quad V_1 = -\frac{\partial \Psi_1}{\partial x}, \tag{21}$$

and since both the leading-order and perturbation velocity fields are irrotational, Ψ_1 satisfies the Laplace equation, as well as

$$\Psi_1 \sim -U_e \delta^* \quad \text{as} \quad Y \to 0, \tag{22}$$

which follows from (18). The solution for Ψ_1 is

$$\Psi_1(x, Y, t) = -\frac{1}{\pi}\int_{-\infty}^{\infty} \frac{Y U_e(s,t)\,\delta^*(s,t)}{(s-x)^2 + Y^2}\, ds, \tag{23}$$

and it can then be shown that, in general,

$$U_1 = -\frac{1}{\pi}\int_{-\infty}^{\infty} \frac{(s-x)\,V_d(s,t)}{(s-x)^2+Y^2}\,ds, \tag{24}$$

$$V_1 = \frac{1}{\pi}\int_{-\infty}^{\infty} \frac{YV_d(s,t)}{(s-x)^2+Y^2}\,ds. \tag{25}$$

To evaluate the specific leading-order inviscid flow of interest here, define a stream function Ψ_0 such that $U_0 = \partial\Psi_0/\partial Y$, $V_0 = -\partial\Psi_0/\partial x$. For a vortex whose instantaneous location is at $\{X_v(t), Y_v(t)\}$, Ψ_0 is given by

$$\Psi_0 = -\log\left\{\frac{(x-X_v(t))^2+(Y-Y_v(t))^2}{(x-X_v(t))^2+(Y+Y_v(t))^2}\right\}, \tag{26}$$

and it is easily verified by differentiation that the velocity components of the vortex centre are given by

$$U_v(t) = \frac{dX_v}{dt} = \frac{1}{Y_v}, \quad V_v(t) = \frac{dY_v}{dt} = 0, \tag{27}$$

to leading order. Viewed from the laboratory frame, the inviscid motion is unsteady as the vortex moves above the wall. For the limit problem $Re \to \infty$ (see Part 1) the inviscid motion is steady to an observer who moves uniformly with the vortex. In the IBL calculations, the thickening boundary layer influences the trajectory of the vortex, but it is nevertheless convenient to transform to the vortex frame which convects to the right with speed $U_v(t)$. If x is now understood to measure streamwise distance in the vortex frame from the vortex centre, the stream function in this frame is

$$\Psi_0 = -YU_v(t) - \log\left\{\frac{x^2+(Y-Y_v)^2}{x^2+(Y+Y_v)^2}\right\}, \tag{28}$$

to leading order.

The inviscid mainstream velocity at the boundary-layer edge in the moving vortex frame is denoted by $U_\infty(x,t)$, while $U_e(x,t)$ is the instantaneous mainstream distribution in the laboratory reference frame; the two distributions are related by

$$U_\infty(x,t) = -U_v(t) + U_e(x,t). \tag{29}$$

A first approximation to U_e may be obtained by differentiating (28), and, to leading order,

$$U_e(x,t) = \frac{4Y_v}{x^2+Y_v^2} + \ldots. \tag{30}$$

In an interacting boundary-layer approach, a specific finite but large value of the Reynolds number is adopted and the $O(Re^{-\frac{1}{2}})$ corrections to the inviscid flow induced by the boundary layer are evaluated. In the present situation, both the vortex trajectory and the velocity at the boundary-layer edge are influenced. The corrections to (27) can be calculated by evaluation of (24) and (25) at the vortex location, and it can be shown that

$$U_v(t) = \frac{1}{Y_v(t)} - \frac{Re^{-\frac{1}{2}}}{\pi}\int_{-\infty}^{\infty} \frac{sV_d(s,t)}{s^2+Y_v^2}\,ds, \tag{31}$$

$$V_v(t) = \frac{Re^{-\frac{1}{2}}Y_v(t)}{\pi}\int_{-\infty}^{\infty} \frac{V_d(s,t)}{s^2+Y_v^2}\,ds, \tag{32}$$

where the displacement velocity is given by (19). The normal coordinate of the vortex Y_v is evaluated from

$$\frac{dY_v}{dt} = V_v(t), \quad Y_v(0) = 1, \tag{33}$$

with the initial condition reflecting the lengthscale used to define dimensionless variables. The correction to the velocity U_e in (30) is evaluated by taking the limit $Y \to 0$ in (24) and it follows that

$$U_e(x,t) = \frac{4Y_v(t)}{x^2+Y_v^2} + \frac{Re^{-\frac{1}{2}}}{\pi}\int_{-\infty}^{\infty} \frac{V_d(s,t)}{x-s}\,ds, \tag{34}$$

where the integral in (34) must be interpreted as a Cauchy principal-value integral. Note that the IBL procedure is only justified in situations where the second term on the right-hand side of (34) remains small with respect to the first.

3. Lagrangian boundary-layer equations

The interacting boundary layer (IBL) algorithm used here consists of two coupled sets of calculations at each time step, one to evaluate the development of the boundary layer and one to compute the influence of the thickening boundary layer on the external flow. The boundary-layer problem was formulated in Lagrangian variables, wherein the coordinates (ξ, η) of a large number of fluid particles at some initial instant in time are used as independent spatial variables. The current position of each fluid particle (x, y), as well as its current components of velocity (u, v) are functions of (ξ, η, t), corresponding to where the fluid particle started in space and the elapsed time along its trajectory. The boundary-layer portion of the formulation is similar to that described in Part 1 except that the mainstream flow in the vortex frame is now unsteady, as well as the speed of the wall which moves to the left with velocity $-U_v(t)$. The boundary-layer equations in Lagrangian coordinates are:

$$\frac{\partial u}{\partial t} = \frac{\partial U_\infty}{\partial t} + U_\infty \frac{\partial U_\infty}{\partial x} + \left(\frac{\partial x}{\partial \xi}\frac{\partial}{\partial \eta} - \frac{\partial x}{\partial \eta}\frac{\partial}{\partial \xi}\right)^2 u, \tag{35}$$

$$\frac{\partial x}{\partial t} = u. \tag{36}$$

In (35), $U_\infty(x,t)$ is the mainstream velocity distribution in the vortex frame according to (29), which is determined during the course of the calculation using (34). The boundary conditions for this system for all $t > 0$ are

$$u = -U_v(t) \quad \text{at} \quad \eta = 0; \qquad u \to U_\infty(x,t) \quad \text{as} \quad \eta \to \infty. \tag{37}$$

The initial conditions are that the streamwise velocity distribution is known at some initial instant at $t = t_0$, namely

$$u = u_0(\xi, \eta) \quad \text{at} \quad t = t_0 \tag{38}$$

for known fluid particle locations in the boundary layer

$$x(\xi, \eta, t) = \xi, \quad y(\xi, \eta, t) = \eta \quad \text{at} \quad t = t_0. \tag{39}$$

A Lagrangian integration may be initiated at any time when the velocity field is known. In the present study, the motion was impulsively started from rest at $t = 0$ and, for a Lagrangian integration initiated at this time,

$$U_v = Y_v = 1, V_v = 0 \qquad \text{at } t = 0, \tag{40}$$

$$U_e(x, 0) = U_{e0}(x) = \frac{4}{x^2+1} \quad \text{at } t = 0, \tag{41}$$

and $u_0 = -1 + U_{e0}(x)$ in (38) for $t_0 = 0$. In the early stages of the motion, the boundary-layer flow is well-behaved and it is somewhat easier (and more accurate just after the impulsive start) to compute the development using a conventional interactive Eulerian formulation. This was carried out for a range of Reynolds numbers and the results from both integration procedures were found to agree well. In fact, the boundary layer in the initial development is very thin and interactive effects were found to be small; the results of the interactive calculations over a range of Re were found to be indistinguishable (at least up to $t = 0.25$), from the results produced in the non-interactive limit-problem computations discussed in Part 1. For this reason the interactive calculations described here were generally started at $t_0 = 0.25$, starting with conditions (39) and (40) and using the velocity field u produced from the results of the Eulerian integration for the limit problem $Re \to \infty$ over the interval $0 \leqslant t \leqslant t_0$. The specific value of t_0 used is arbitrary as long as t_0 is small and the effects of interaction are small.

In the interactive problem, it is necessary to evaluate the displacement thickness, δ^*, at each time step in order to calculate the displacement velocity V_d in (19) and the consequent influence on the external flow distribution in (34); this is defined in terms of velocities in the laboratory frame by

$$\delta^*(x, t) = \int_0^\infty \left\{1 - \frac{u + U_v(t)}{U_e(x, t)}\right\} dy. \tag{42}$$

It is noted in passing that u in this equation is defined in the moving vortex frame, as opposed to the conventional definition of δ^* in (17) where u is relative to the laboratory frame. To calculate δ^* it is necessary to evaluate the y particle positions through integration of the continuity equation in Lagrangian coordinates, which is

$$\frac{\partial x}{\partial \xi}\frac{\partial y}{\partial \eta} - \frac{\partial x}{\partial \eta}\frac{\partial y}{\partial \xi} = 1. \tag{43}$$

This equation is a first-order equation for $y(\xi, \eta, t)$ and, for a given distribution of $x(\xi, \eta, t)$, can be integrated along the characteristic curves which are contours of constant x. The integral in (42) is taken with $x =$ constant and thus a numerical integration along a specific characteristic of (43) provides the necessary values of y and u to compute δ^*. The method will be described subsequently in §5.

4. Numerical solution of the boundary-layer problem

To advance the solution of (35) and (36) forward in time, it was convenient to work in terms of variables defined on fixed finite intervals through the following transformations. The streamwise velocity $u(\xi, \eta, t)$ was defined in terms of a normalized variable U by

$$u(\xi, \eta, t) = -U_v(t) + U_e(x, t)\, U(\xi, \eta, t), \tag{44}$$

and therefore the boundary conditions (37) become

$$U = 0 \quad \text{at} \quad \eta = 0, \qquad U \to 1 \quad \text{as} \quad \eta \to \infty. \tag{45}$$

As discussed in Part 1 the dependent and independent streamwise variables x, ξ (defined on the interval $(-\infty, \infty)$) were mapped to the variables $\hat{x}, \hat{\xi}$ defined on the interval $(2, 0)$ by

$$\hat{x} = 1 - \frac{2}{\pi}\arctan x, \quad \hat{\xi} = 1 - \frac{2}{\pi}\arctan \xi. \tag{46}$$

In addition, the normal dependent variable y and independent variable η (defined on the interval $(0, \infty)$) were mapped to the variables $\hat{y}, \hat{\eta}$ defined on the interval $(0, 1)$ by

$$\hat{y} = \frac{2}{\pi}\arctan y, \quad \hat{\eta} = \frac{2}{\pi}\arctan \eta. \tag{47}$$

The transformations (46) and (47) introduce the two functions

$$Z(\hat{y}) = (1 + \cos \pi\hat{y})/\pi, \quad U_{e0}(\hat{x}) = 2(1 - \cos \pi\hat{x}), \tag{48}$$

into the governing equations. Here the subscript 0 in (48) is used to reflect the fact that U_{e0} corresponds to the distribution of U_e at $t = 0$, or alternatively at any stage before the effects of interaction become important; consequently, it is the non-interactive mainstream distribution used in Part 1.

When these transformations are introduced in (35) and (36), it is easily shown that

$$\frac{\partial U}{\partial t} = R\frac{\partial^2 U}{\partial \hat{\xi}^2} + S\frac{\partial^2 U}{\partial \hat{\xi}\,\partial \hat{\eta}} + T\frac{\partial^2 U}{\partial \hat{\eta}^2} + P\frac{\partial U}{\partial \hat{\eta}} + Q\frac{\partial U}{\partial \hat{\xi}} + WU + \Gamma, \tag{49}$$

$$\frac{\partial \hat{x}}{\partial t} = \frac{U_{e0}}{2\pi}\left\{U_v(t) - U_e(\hat{x}, t)\, U(\hat{\xi}, \hat{\eta}, t)\right\}. \tag{50}$$

The functional coefficients in (49) are given by

$$R = \alpha^2\left(\frac{\partial \hat{x}}{\partial \hat{\eta}}\right)^2, \quad S = -2\alpha^2\left(\frac{\partial \hat{x}}{\partial \hat{\xi}}\right)\left(\frac{\partial \hat{x}}{\partial \hat{\eta}}\right), \quad T = \alpha^2\left(\frac{\partial \hat{x}}{\partial \hat{\xi}}\right)^2, \tag{51}$$

$$P = \alpha^2\left\{\frac{\partial \hat{x}}{\partial \hat{\xi}}\left(\frac{\partial^2 \hat{x}}{\partial \hat{\xi}\,\partial \hat{\eta}} + \beta(\hat{\eta})\frac{\partial \hat{x}}{\partial \hat{\xi}}\right) - \frac{\partial \hat{x}}{\partial \hat{\eta}}\left(\frac{\partial^2 \hat{x}}{\partial \hat{\xi}^2} + \gamma(\hat{\xi})\frac{\partial \hat{x}}{\partial \hat{\xi}}\right)\right\}, \tag{52}$$

$$Q = \alpha^2\left\{\frac{\partial \hat{x}}{\partial \hat{\eta}}\left(\frac{\partial^2 \hat{x}}{\partial \hat{\xi}\,\partial \hat{\eta}} + \gamma(\hat{\xi})\frac{\partial \hat{x}}{\partial \hat{\eta}}\right) - \frac{\partial \hat{x}}{\partial \hat{\xi}}\left(\frac{\partial^2 \hat{x}}{\partial \hat{\eta}^2} + \beta(\hat{\eta})\frac{\partial \hat{x}}{\partial \hat{\eta}}\right)\right\}, \tag{53}$$

$$W = -\frac{1}{2\pi}\frac{U_{e0}(\hat{x})}{U_e(\hat{x}, t)}\frac{\partial U_e}{\partial \hat{x}}\left\{U_v(t) - U_e(x, \hat{t})\, U(\hat{\xi}, \hat{\eta}, t)\right\} - \frac{1}{U_e}\frac{\partial U_e}{\partial t}, \tag{54}$$

$$\Gamma = \frac{1}{2\pi}\frac{U_{e0}(\hat{x})}{U_e(\hat{x}, t)}\frac{\partial U_e}{\partial \hat{x}}\left\{U_v(t) - U_e(\hat{x}, t)\right\} + \frac{1}{U_e}\frac{\partial U_e}{\partial t}. \tag{55}$$

In these equations

$$\alpha(\hat{x}, \hat{\xi}, \hat{\eta}) = \frac{U_{e0}(\hat{\xi})}{U_{e0}(\hat{x})}Z(\hat{\eta}), \tag{56}$$

and
$$\beta(\hat{\eta}) = \frac{Z'(\hat{\eta})}{Z(\hat{\eta})}, \quad \gamma(\hat{\xi}) = \frac{U'_{e0}(\hat{\xi})}{U_{e0}(\hat{\xi})}, \tag{57}$$

where a prime indicates differentiation with respect to the appropriate variable. The boundary conditions for (49) and (50) are

$$U = 0 \quad \text{at} \quad \hat{\eta} = 0, \qquad U \to 1 \quad \text{as} \quad \hat{\eta} \to 1, \tag{58}$$

$$\hat{x} = 0 \quad \text{at} \quad \hat{\xi} = 0, \qquad \hat{x} = 2 \quad \text{at} \quad \hat{\xi} = 2. \tag{59}$$

It should be noted that (59) reflects the fact that fluid particles initially at infinity remain there. Furthermore $\hat{x} \sim \hat{\xi}$ as $\hat{\xi} \to 0, 2$ and it is readily shown that all coefficients in (49) vanish except for T and P; it may then be verified that

$$U = \operatorname{erf}\left(\frac{\tan(\frac{1}{2}\pi\hat{\eta})}{2t^{\frac{1}{2}}}\right) \quad \text{at} \quad \hat{\xi} = 0, 2. \tag{60}$$

Consequently, U is known all around the boundary of the computational domain. Fluid particles on the wall and at the mainstream remain there, but their streamwise position changes with time and the values of $\hat{x}$ on $\hat{\eta} = 0, 1$ at any time are readily computed from (50).

The interacting boundary-layer problem was solved iteratively at each time step. The principal numerical scheme to advance the boundary-layer solution for $0 < \hat{\xi} < 2$ and $0 < \hat{\eta} < 1$ is the upwind–downwind alternating-direction-implicit (ADI) method described in Part 1 for integration of the limit problem $Re \to \infty$ (see also Peridier & Walker 1988). The main difference in the computational algorithm here is that an additional iteration is necessary to compute $U_e(\hat{x}, t)$ at each time step from the interaction condition; this aspect will be discussed in §5. If, however, it is assumed that an estimate of $U_e(\hat{x}, t)$ is available at any stage in the current time plane, the coefficients in (51)–(55) may be evaluated and the iterative ADI method of Part 1 can be implemented. Numerical integrations were carried out with two sets of meshes using 61×41 and then 101×61 mesh points in the $\hat{\xi}, \hat{\eta}$ directions respectively. Agreement between the two sets of calculations was good (as also confirmed by recent calculations by Lou 1990 on a 201×101 mesh) and the results presented here are based on the smallest set of mesh sizes used ($\Delta\hat{\xi} = 0.02$, $\Delta\hat{\eta} = 0.0167$). The time step was typically taken small with $\Delta t = O(10^{-3})$ initially, in order to keep the number of iterations at a reasonable level; as the solution for each value of Re approached a singular behaviour, the time step was continually reduced. The convergence test was rather restrictive and required that successive iterates for U agree to within four significant figures at all points in the mesh; this condition was typically satisfied in 3–10 iterations per time step.

5. Numerical solution of the interaction condition

The external flow distribution in an IBL formulation is influenced by the changing boundary-layer thickness and the central feature derived from the boundary-layer calculation is the displacement-thickness distribution which, from (42) and (44), is given by

$$\delta^*(x, t) = \int_0^\infty \{1 - U(\xi, \eta, t)\}\, dy. \tag{61}$$

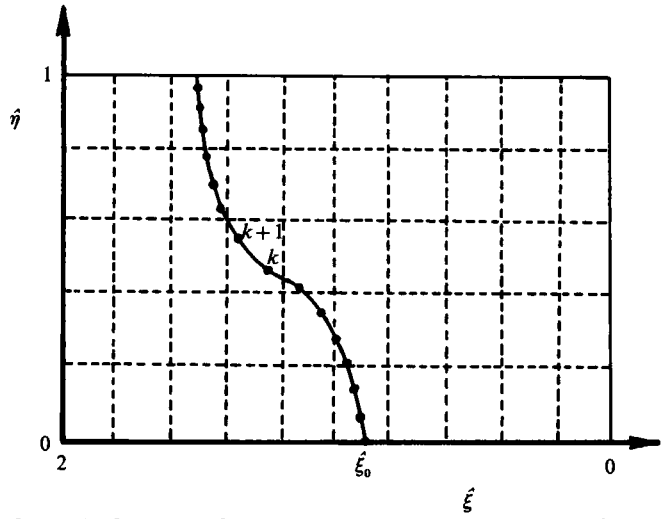

FIGURE 3. Schematic diagram of integration along a characteristic $\hat{x}$ = constant in the $(\hat{\xi}, \hat{\eta})$-plane starting from a point on the wall at $\hat{\xi}_0$.

In terms of the transformed variables

$$\delta^*(\hat{x}, t) = \int_0^1 \frac{1-U}{Z(\hat{y})} \mathrm{d}\hat{y}, \tag{62}$$

where the integral in (62) must be carried out along a path with $\hat{x}$ constant. Such paths are characteristics of the continuity equation (43), which in transformed variables is

$$A\frac{\partial \hat{y}}{\partial \hat{\xi}} + B\frac{\partial \hat{y}}{\partial \hat{\eta}} = C, \tag{63}$$

where

$$A = -\frac{\partial \hat{x}}{\partial \hat{\eta}}, \quad B = \frac{\partial \hat{x}}{\partial \hat{\xi}}, \quad C = \frac{U_{e0}(\hat{x})\, Z(\hat{y})}{U_{e0}(\hat{\xi})\, Z(\hat{\eta})}. \tag{64}$$

The subsidiary equations are

$$\frac{\mathrm{d}\hat{\xi}}{A} = \frac{\mathrm{d}\hat{\eta}}{B} = \frac{\mathrm{d}\hat{y}}{C} = \mathrm{d}\hat{s}, \tag{65}$$

where $\hat{s}$ is a variable along the characteristic curves $\hat{x}$ = constant. For a given distribution of $\hat{x}(\hat{\xi}, \hat{\eta}, t)$ at time t, an integration of (65) may be initiated at the wall to generate a sequence of points $(\hat{\xi}^k, \hat{\eta}^k)$, $k = 1, 2, 3, \ldots$, defining a particular contour $\hat{x}$ = constant; this integration also establishes the corresponding values of $\hat{y}^k$ along the contour and makes possible the integration indicated in (62) to find δ^*. Let A^k and B^k be the values of A and B at the kth point on the contour, as illustrated schematically in figure 3. The step size in $\hat{s}$ along the contour, from the kth point to the point $(k+1)$ was selected so that

$$\Delta\hat{s} = \frac{\Delta\hat{\xi}}{[(A^k)^2 + (B^k)^2]^{\frac{1}{2}}}, \tag{66}$$

which restricts the step along the contour to one mesh length in $\hat{\xi}$. This step size was determined to be sufficiently small to ensure accurate evaluation of $\hat{y}$ and δ^*.

The subsidiary equations (65) were integrated from the wall in a step-by-step manner using a predictor–corrector method. Assume that the $\hat{y}^k$ is known at the kth point on a constant-$\hat{x}$ contour at $(\hat{\xi}^k, \hat{\eta}^k)$ and the object is to calculate the solution at the point $k+1$. To obtain predicted values of $(\hat{\xi}^{k+1}, \hat{\eta}^{k+1})$, the coefficients in (64) were evaluated at $(\hat{\xi}^k, \hat{\eta}^k)$. It is, in general, necessary to evaluate these coefficients at locations which are not at a mesh point in the $(\hat{\xi}, \hat{\eta})$-plane. To accomplish this task at any point in the procedure, a four-point bivariate interpolation formula (Abramowitz & Stegun 1964, p. 882) was used with the four points in the mesh surrounding the point in question; the gradients in A and B were evaluated using central differences. The corrector formula used was

$$\hat{y}^{k+1} = \hat{y}^k + \tfrac{1}{2}\Delta\hat{s}\{C^{k+1} + C^k\}, \tag{67}$$

for $\hat{y}^{k+1}$, for example, with similar approximations to (64) being obtained for $\hat{\xi}^{k+1}$ and $\hat{\eta}^{k+1}$. The corrector algorithm is second-order accurate in $\Delta\hat{s}$ and the step size used was small enough so that only a single application of the corrector was necessary at each step. As the integration proceeds along the constant-$\hat{x}$ characteristics, values of U at $(\hat{\xi}^k, \hat{\eta}^k)$ were obtained by bivariate interpolation of the solution of (49) at the current time t. The displacement thickness δ^* was obtained using these values by evaluating the right-hand side of (62) with an integration procedure based on the trapezoidal rule. In practice, the integration for δ^* along the characteristic was terminated once the integrand in (62) was sufficiently small; consequently, each integration was generally stopped before the line $\hat{\eta} = 1$ was reached. By carrying out an integration along several characteristics, values of δ^* were obtained at a number of values of $\hat{x}$ that define a mesh in $\hat{x}$ for the outer inviscid problem. In principle, there is no reason why the mesh spacing in $\hat{\xi}$ need correspond to that in $\hat{x}$, other than for convenience; in the present study sufficient integrations of (65) were carried out to define a displacement-thickness distribution on an 'outer' mesh with $\Delta\hat{x} = \Delta\hat{\xi}$.

At a given time t, once an estimate of $\delta^*(\hat{x}, t)$ is available, the velocity components of the vortex can be estimated from (31) and (32) which become

$$U_{\mathrm{v}}(t) = \frac{1}{Y_{\mathrm{v}}(t)} + \frac{Re^{-\frac{1}{2}}}{\pi}\int_0^2 \frac{\tan\frac{1}{2}\pi(1-\hat{x})\,(\delta^* U_{\mathrm{e}})'}{\tan^2\{\frac{1}{2}\pi(1-\hat{x})\} + Y_{\mathrm{v}}^2}\,\mathrm{d}\hat{x}, \tag{68}$$

$$V_{\mathrm{v}}(t) = -\frac{Y_{\mathrm{v}}(t)\,Re^{-\frac{1}{2}}}{\pi^{\frac{1}{2}}}\int_0^2 \frac{(\delta^* U_{\mathrm{e}})'}{\tan^2\{\frac{1}{2}\pi(1-\hat{x})\} + Y_{\mathrm{v}}^2}\,\mathrm{d}\hat{x}, \tag{69}$$

where a prime denotes differentiation with respect to $\hat{x}$. With estimates of δ^* and U_{e} available on a mesh defined by

$$\hat{x}_i = i\Delta\hat{x}, \quad i = 0, 1, 2, \ldots, N, \tag{70}$$

where $\Delta\hat{x} = 2/N$ and N is the total number of subdivisions, the vortex velocity components were evaluated by integrating (68) and (69) using the trapezoidal rule and central differences to compute the derivatives. The current distance of the vortex from the wall was then computed from the following approximation to (33):

$$Y_{\mathrm{v}} = Y_{\mathrm{v}}^* + \tfrac{1}{2}\Delta t(V_{\mathrm{v}} + V_{\mathrm{v}}^*). \tag{71}$$

Here the asterisk denotes values in the previous time plane at $t^* = t - \Delta t$. It is worth commenting that the influence of the boundary layer on the trajectory of the vortex was found to be very small for all Reynolds numbers over the time intervals

considered in this study; departures from the steady values of $Y_v = 1$, $U_v = 1$, $V_v = 0$, that are appropriate for the limit problem $Re \to \infty$ (Part 1), were slight.

In contrast, the computed inviscid velocity distribution $U_e(\hat{x}, t)$ was found to develop substantial deviations from the limit-problem ($Re \to \infty$) distribution in a very narrow streamwise band near the location where a boundary-layer eruption develops. It may be inferred from (19) and (34) that, in an interactive boundary-layer approach, U_e satisfies an integro-differential equation involving a Cauchy principal-value integral. The accurate and efficient evaluation of U_e at each time step was found to be the most critical, as well as the most challenging, aspect of the IBL computations. Define a general Cauchy integral on an infinite domain by

$$C(x,t) = \frac{1}{\pi}\int_{-\infty}^{\infty} \frac{F(s,t)\,\mathrm{d}s}{x-s}, \tag{72}$$

where in this study

$$F(x,t) = \frac{\partial}{\partial x}\{U_e(x,t)\,\delta^*(x,t)\}. \tag{73}$$

The interaction condition (34) may now be written in the form

$$U_e(x,t) = \frac{4Y_v}{x^2+Y_v^2} + Re^{-\frac{1}{2}}C(x,t). \tag{74}$$

In conventional IBL computations, the distribution of U_e is estimated from the previous iteration in order to compute $C(x,t)$ in (72) and hence define the next iterate for U_e. In view of the fact that U_e eventually develops intense local variations in both space and time in the present problem, this approach proved unacceptably slow. In addition, the standard method of assuming that F in (73) may be approximated as constant over each subinterval of the indicated integration is only first order accurate in Δs (Napolitano, Werle & Davis 1978); such schemes were found to be very inaccurate in the present calculations where the displacement surface develops a 'spike' distribution. For these reasons, some care was taken to develop a second-order-accurate method for the Cauchy integral (similar to that described by Napolitano *et al.* 1978), as well as an efficient method to compute $U_e(x,t)$ from (74).

In a quasi-steady approach, t is held fixed at any stage and, omitting the time dependence, the evaluation of the Cauchy integral (72) at a typical point x_i in the mesh is considered. The integral was split into two parts according to

$$C(x_i) = S(x_i) + L(x_i), \tag{75}$$

where S_i is the main part of the integral defined by

$$S_i = S(x_i) = \frac{1}{\pi}\int_{-R}^{R} \frac{F(s)\,\mathrm{d}s}{x_i - s}, \tag{76}$$

R is a large fixed value of x to be selected and L_i represents the asymptotic tails of the integral, namely

$$L_i = L(x_i) = \frac{1}{\pi}\left\{\int_{R}^{\infty} \frac{F(s)}{x_i - s}\mathrm{d}s + \int_{-\infty}^{-R} \frac{F(s)}{x_i - s}\mathrm{d}s\right\}. \tag{77}$$

The distributions U_e and δ^* were evaluated as functions of $\hat{x}$ defined on the interval $(0, 2)$ using the discretization in (70). The contributions to C for large x (i.e. for $\hat{x}$ near

0 or 2) were evaluated using (77), while the integral in (76) was written in terms of $\hat{x}$ according to

$$S_i = \frac{1}{\pi}\sin(\tfrac{1}{2}\pi\hat{x}_i)\int_{\epsilon}^{2-\epsilon}\frac{H(\hat{s})}{\sin\{\tfrac{1}{2}\pi(\hat{x}_i-\hat{s})\}}\,\mathrm{d}\hat{s}. \tag{78}$$

Values of R and ϵ were selected as

$$\epsilon = \tfrac{1}{2}\Delta\hat{x}, \quad R = \tan\{\tfrac{1}{2}\pi(1-\tfrac{1}{2}\Delta\hat{x})\}, \tag{79}$$

and $H(\hat{x})$ is given by

$$H(\hat{x}) = \sin(\tfrac{1}{2}\pi\hat{x})\frac{\partial}{\partial\hat{x}}(U_e\delta^*). \tag{80}$$

Equation (78) may be written as the sum of integrals

$$S_i = \frac{1}{\pi}\sin(\tfrac{1}{2}\pi\hat{x}_i)\sum_{j=1}^{N-1}\int_{\hat{x}_j-\epsilon}^{\hat{x}_j+\epsilon}\frac{H(\hat{s})}{\sin\{\tfrac{1}{2}\pi(\hat{x}_i-\hat{s})\}}\,\mathrm{d}\hat{s}, \tag{81}$$

and it may be noted that the nodes $\hat{x}_j$ are at the midpoints of the corresponding interval of integration. The simplest approach to evaluating (81) is to assume that $H(\hat{s})$ is constant over each interval and equal to the value at the nodal point $\hat{x}_j$ (see, for example, Henkes & Veldman 1987 and Riley & Vasantha 1989). However, as noted by Napolitano *et al.* (1978), such schemes are only first-order accurate in $\Delta\hat{x}$. To obtain a second-order method, take

$$H(\hat{x}_j) = H_j + (\hat{x}-\hat{x}_j)H_j', \tag{82}$$

on the jth interval $(\hat{x}_j-\epsilon, \hat{x}_j+\epsilon)$; here H_j' denotes the first derivative of H evaluated at $\hat{x}_j$. The work of Napolitano *et al.* (1978) shows that a representation of the form (82) leads to second-order accuracy for $C(x_i)$. The following second-order-accurate formulae were used to evaluate H_j and H_j' from (80):

$$H_j = \frac{\sin(\frac{1}{2}\pi\hat{x}_j)}{2\Delta\hat{x}}\{(\delta^*U_e)_{j+1}-(\delta^*U_e)_{j-1}\}, \tag{83}$$

$$H_j' = \frac{\pi\cos(\frac{1}{2}\pi\hat{x}_j)}{4\Delta\hat{x}}\{(\delta^*U_e)_{j+1}-(\delta^*U_e)_{j-1}\}+\frac{\sin(\frac{1}{2}\pi\hat{x}_j)}{(\Delta\hat{x})^2}\{(\delta^*U_e)_{j+1}-2(\delta^*U_e)_j+(\delta^*U_e)_{j-1}\}. \tag{84}$$

A second-order-accurate approximation to (78) is the form

$$S_i = \frac{1}{\pi}\sin(\tfrac{1}{2}\pi\hat{x}_i)\sum_{j-1}^{N-1}\{\alpha_{ij}H_j+\beta_{ij}H_j'\}, \tag{85}$$

where formulae for the constants α_{ij} and β_{ij} are given in the Appendix. It should be noted that finite-difference representations of H_j and H_j' other than (83) and (84) are possible and several alternatives were tried. In particular, as a 'spike' starts to develop in the displacement-thickness distribution, (83) and (84) may potentially be applied across the spike. Therefore, a number of attempts were made to isolate the current streamwise location of the spike that developed in the latter stages of the integrations, and to implement one-sided difference formulae on either side. However, these procedures did not change the results significantly, and since they involved substantially more computation, the bulk of the calculations were based on (83) and (84).

Consider now the tail portions of the Cauchy integral in (77). For $|x|$ large the solution for U approaches the plane-parallel flow given by (60), and it can be shown using (61) that

$$\delta^*(\hat{x},t) \to \delta^*_\infty(t) = 2(t/\pi)^{\frac{1}{2}} \quad \text{as} \quad |x| \to \infty. \tag{86}$$

Since the strong interactions occur in regions where x is $O(1)$, the dominant part of U_e is given by the first term on the right-hand side of (34), and it is easily shown from (34) and (73) that

$$F \sim \frac{u_3}{x^3} + \frac{u_5}{x^5} \ldots \quad \text{as} \quad |x| \to \infty, \tag{87}$$

where

$$u_3 = -8Y_v(t)\,\delta^*_\infty(t), \quad u_5 = -2u_3\,Y_v^2. \tag{88}$$

It follows from the results in the Appendix that L_i in (77) is closely approximated by

$$L_i \sim u_3\{a_3(x_i) + b_3(x_i)\} + u_5\{a_5(x_i) + b_5(x_i)\} + \ldots, \tag{89}$$

where the a_j and b_j are given in the Appendix.

Upon substitution of (83), (84), (85) and (89) into the interaction condition (74), it may be confirmed that, for a given distribution of δ^*, a set of linear algebraic equations for U_{e_i} $(i = 1, 2, \ldots, N-1)$ is obtained, which may be represented in matrix form as

$$(\boldsymbol{I} - \boldsymbol{M})\,\boldsymbol{U}_e = \boldsymbol{A}. \tag{90}$$

Here $\boldsymbol{I}$ is the identity matrix and $\boldsymbol{M}$ is the coefficient matrix defined by

$$M_{ij} = \frac{\delta^*_j S_i Re^{-\frac{1}{2}}}{2\pi\Delta\hat{x}}\Big\{\alpha_{i,j-1}S_{j-1} - \alpha_{i,j+1}S_{j+1} + \tfrac{1}{2}\pi(\beta_{i,j-1}C_{j-1} - \beta_{i,j+1}C_{j+1}) + \frac{2}{\Delta\hat{x}}(\beta_{i,j+1}S_{j+1} - 2\beta_{ij}S_j + \beta_{i,j-1}S_{i,j-1})\Big\}, \tag{91}$$

where

$$S_j = \sin(\tfrac{1}{2}\pi\hat{x}_j), \quad C_j = \cos(\tfrac{1}{2}\pi\hat{x}_j). \tag{92}$$

Note that $U_{e_0} = U_{e_N} = 0$, and in (91)

$$\alpha_{i,0} = \alpha_{i,N} = \beta_{i,0} = \beta_{i,N} = 0. \tag{93}$$

In (91), $\boldsymbol{U}_e$ represents the vector of values of U_{e_i} to be found at the interior points $i = 1, 2, 3, \ldots, N-1$ and the components of the right-hand side vector are given by

$$A_i = \frac{4Y_v}{\tan^2\{\frac{1}{2}\pi(1-\hat{x}_i)\} + Y_v^2} + Re^{-\frac{1}{2}}\{u_3(a_3(x_i) + b_3(x_i)) + u_5(a_5(x_i) + b_5(x_i))\}, \tag{94}$$

for $i = 1, 2, \ldots, N-1$. At any stage the matrix problem defined by (90) was solved for $\boldsymbol{U}_e$ using LU decomposition with scaled partial pivoting.

To compute the solution forward in time, both the boundary-layer and external-flow problem must be advanced simultaneously, and to accomplish this a predictor–corrector strategy was employed. Assume that the entire solution is known at time t^*. The value U_v^* and the distribution U_e^* were used to estimate the corresponding values at time t and the boundary-layer problem was solved to find 'predicted' distributions of the dependent variables $\hat{x}(\xi, \eta, t)$ and $U(\xi, \eta, t)$ and hence a predicted distribution $\delta^*(\hat{x}, t)$. The predicted displacement thickness was then utilized to solve the outer-flow problem to obtain corrected values of U_v and U_e. A corrected boundary-layer solution was then obtained and the process was iterated

until convergence occurred. This was considered to have occurred when two successive iterates for U agreed to four significant figures at all points in the mesh. Typically 3–10 overall iterations were required per time step.

6. Calculated results

The evolution of the boundary layer was considered for four Reynolds numbers, namely $Re = 10^5$, 10^6, 10^7 and 10^8. In all cases the computed results are virtually indistinguishable from those obtained for the limit problem $Re \to \infty$ discussed in Part 1 until the point in time when a strong interaction begins to develop. Even at this stage, the only major differences from the limit solution ($Re \to \infty$) occur in a narrow streamwise band defining the location where the boundary layer is becoming eruptive. Calculations were carried out for each case until a singularity evolved in the boundary-layer solution. This was determined through a combination of criteria, the first of which involved tracking the location of the minimum of the norm-gradient function,

$$\mathcal{N} = \left(\frac{\partial \hat{x}}{\partial \hat{\xi}}\right)^2 + \left(\frac{\partial \hat{x}}{\partial \hat{\eta}}\right)^2. \tag{95}$$

As discussed in Part 1, $\mathcal{N} \to 0$ as a stationary point forms in the x field. At any time, the position of the particle with minimum $\mathcal{N}(\hat{\xi}_M, \hat{\eta}_M)$ was located as well as the contour of constant $x = x_M$ passing through the point. As t increased, the absolute minimum in $\mathcal{N}$ was observed to decrease monotonically. As in Part 1, a singularity was considered to have occurred once the location of minimum $\mathcal{N}$ reached the zero-vorticity line. As $t \to t_s-$ it was observed that, in accordance with the theory of Smith (1988*a*), the wall shear, as well as $\mathrm{d}p/\mathrm{d}x$ and v at the boundary-layer edge, increased to large values. A summary of the calculated singular times is given in table 1. Here, $t_{0I}(Re)$ is a somewhat subjective quantity defined as the first time a 'spike' was observable in the displacement surface, thus corresponding to the first hint of the onset of strong interaction; following this event all cases proceeded rapidly towards eruption and a singularity at $t_s(Re)$. These times, as well as the streamwise location of the singularity $x_s(Re)$ and the velocity of the singularity $-K(Re)$ (see Elliott *et al.* 1983), are listed in table 1. It is evident that both t_{0I} and t_s decrease with decreasing Reynolds number, and therefore the influence of interaction does not postpone or mitigate the evolution of a singularity but acts to hasten breakdown of the boundary-layer solution. It is also of interest to note that in all cases the singularity is moving upstream (in a direction opposite to the local external flow) at t_s.

In all cases considered, the boundary layer develops a narrow eruptive zone centred on x_s as $t \to t_s$ which may be seen in the temporal evolution of the displacement thickness in figure 4. For large Re, the spike in displacement thickness evolves rapidly near the end of the calculation. The case $Re = 10^7$ is shown in figure 4(*a*) where the similarity between the sharp spike obtained in the limit calculation in Part 1 should be noted. As Re decreases, the abrupt evolution of the spike still occurs, with the only noticeable change in shape being a slight thickening of the base of the spike. It is worthwhile mentioning that in view of the fact that the Reynolds number is now finite (as opposed to the limit problem $Re \to \infty$), the top of the spike is at a finite distance from the surface. At $Re = 10^5$, a new feature enters as illustrated in figure 4(*b*) corresponding to the evolution of a smaller secondary spike to the left of the primary eruptive zone; this aspect will be discussed subsequently in connection with the instantaneous flow patterns.

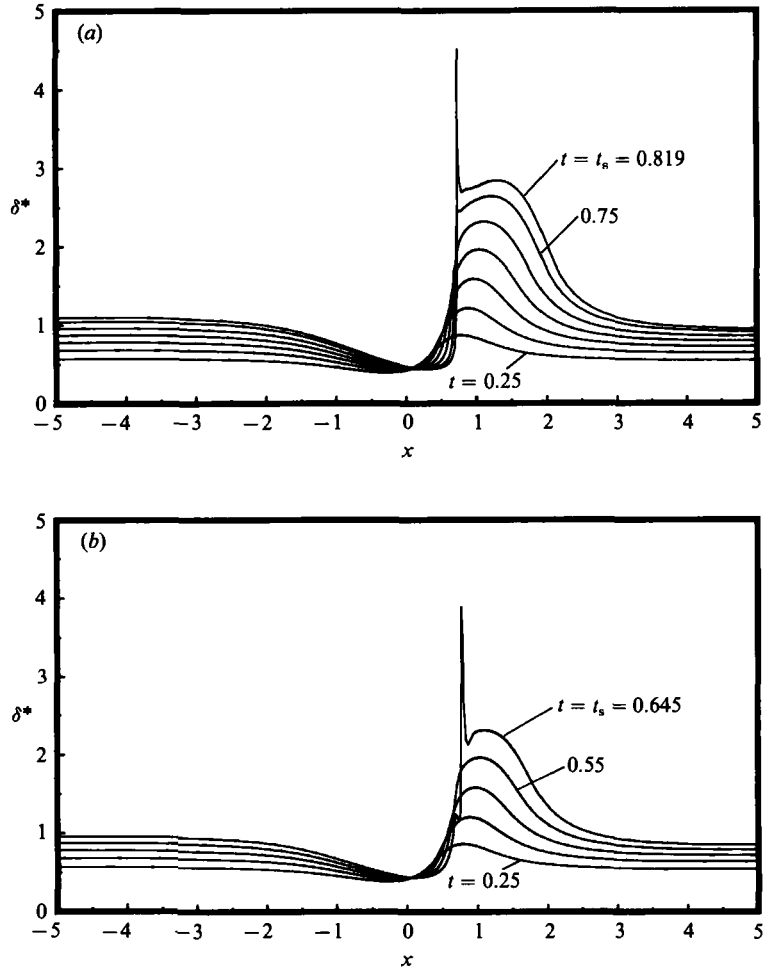

FIGURE 4. Temporal evolution of displacement thickness δ^* at times $t = 0.25$ (0.10) t_s; results are shown in the laboratory reference frame. (*a*) $Re = 10^7$; (*b*) $Re = 10^5$.

Re	t_{0I}	t_s	x_s	$(-K)$
∞	0.890	0.989	−0.214	−0.521
10^8	0.820	0.897	−0.152	−0.686
10^7	0.752	0.819	−0.091	−0.671
10^6	0.680	0.724	0.000	−0.321
10^5	0.623	0.645	0.126	−0.035

TABLE 1. Parameters associated with boundary-layer breakdown, for both the limit problem and interacting studies. Note that x_s and $(-K)$ are in a frame of reference moving with the vortex.

For all the Reynolds numbers considered, the instantaneous streamlines are essentially the same in the early stages of the motion as for the limit problem discussed in Part 1. A complete set of plots is given in Peridier & Walker (1989); only a limited selection will be described here. The instantaneous streamline patterns at $t = t_s$ are shown in figure 5(*a*, *b*) for $Re = 10^6$. The pattern shown in figure 5(*a*) is

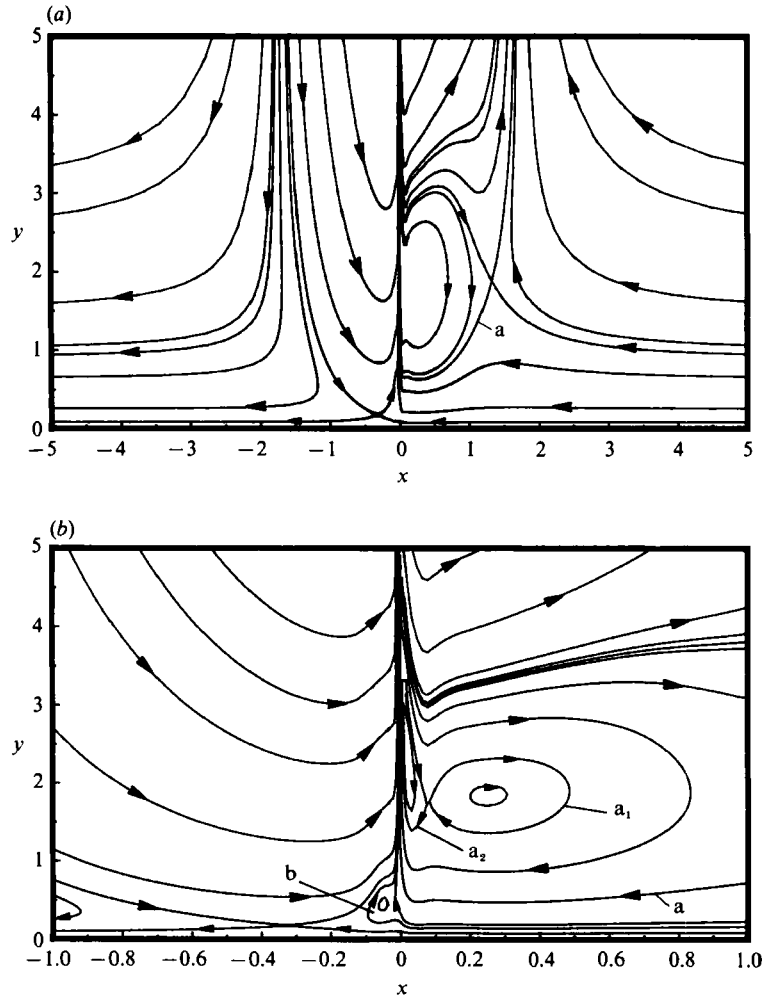

FIGURE 5. Instantaneous streamlines at t_s for $Re = 10^6$; arrows indicate flow direction and (*b*) is on an enlarged streamwise scale.

typical over the entire Reynolds-number range with the flow focusing into the erupting spike on the left-hand side of the secondary eddy. The flow field becomes increasingly complex near the spike as Re decreases. In figure 5(*b*) the flow patterns at t_s are shown on an expanded streamwise scale where it may be seen that the secondary eddy labelled 'a' has split and now contains two inner co-rotating eddies labelled a_1 and a_2. In addition a third tertiary eddy (labelled b) has just formed to the left of the spike.

The instantaneous streamlines for $Re = 10^5$ at t_s are shown in figure 6(*a*) where it may be seen that the secondary eddy (labelled a) is somewhat smaller than for $Re = 10^6$, since the breakdown time $t_s(Re)$ is earlier with decreasing Reynolds number. The tertiary eddy (labelled b) is clearly evident at this time, and in addition to the main interaction associated with the secondary eddy, the instantaneous streamlines are developing a kink due to the tertiary eddy. This is the reason for the second spike in displacement thickness that occurs for $Re = 10^5$ and that was noted in connection with figure 4(*b*). It should be mentioned that a conventional Eulerian algorithm

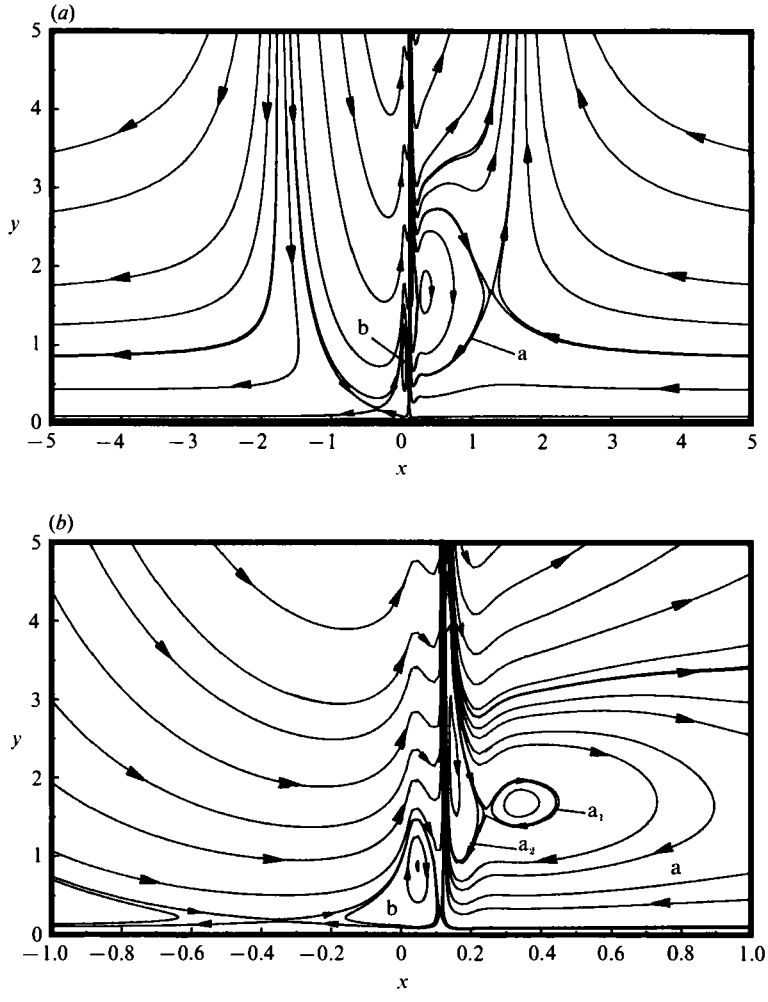

FIGURE 6. Instantaneous streamlines at t_s for $Re = 10^5$; arrows indicate flow direction and (*b*) is on an enlarged streamwise scale.

would probably have great difficulty in coping accurately with the severe flow variations that are evident in figures 5 and 6; however, in the Lagrangian algorithm a large number of fluid particles move into the eruptive zone which is therefore very well resolved. An expanded view of the complex flow patterns that occur near the surface for $Re = 10^5$ is shown in figure 6(*b*) where the co-rotating internal eddies a_1 and a_2 within the secondary eddy and the kinking streamlines due to the tertiary eddy may be seen. The formation of a tertiary eddy has also been found in the interactive calculations of a vortex convected in a uniform flow above a wall (Chuang & Conlisk 1989). Tertiary eddies have also been observed near the surface in an experimental study of the influence of a vortex ring impacting a wall, where both the tertiary and secondary ring were ultimately ejected from the boundary layer in a strong viscous–inviscid interaction (Walker *et al.* 1987).

Finally, the temporal development of the wall shear

$$\tau_w = \left.\frac{\partial u}{\partial y}\right|_{y=0}, \tag{96}$$

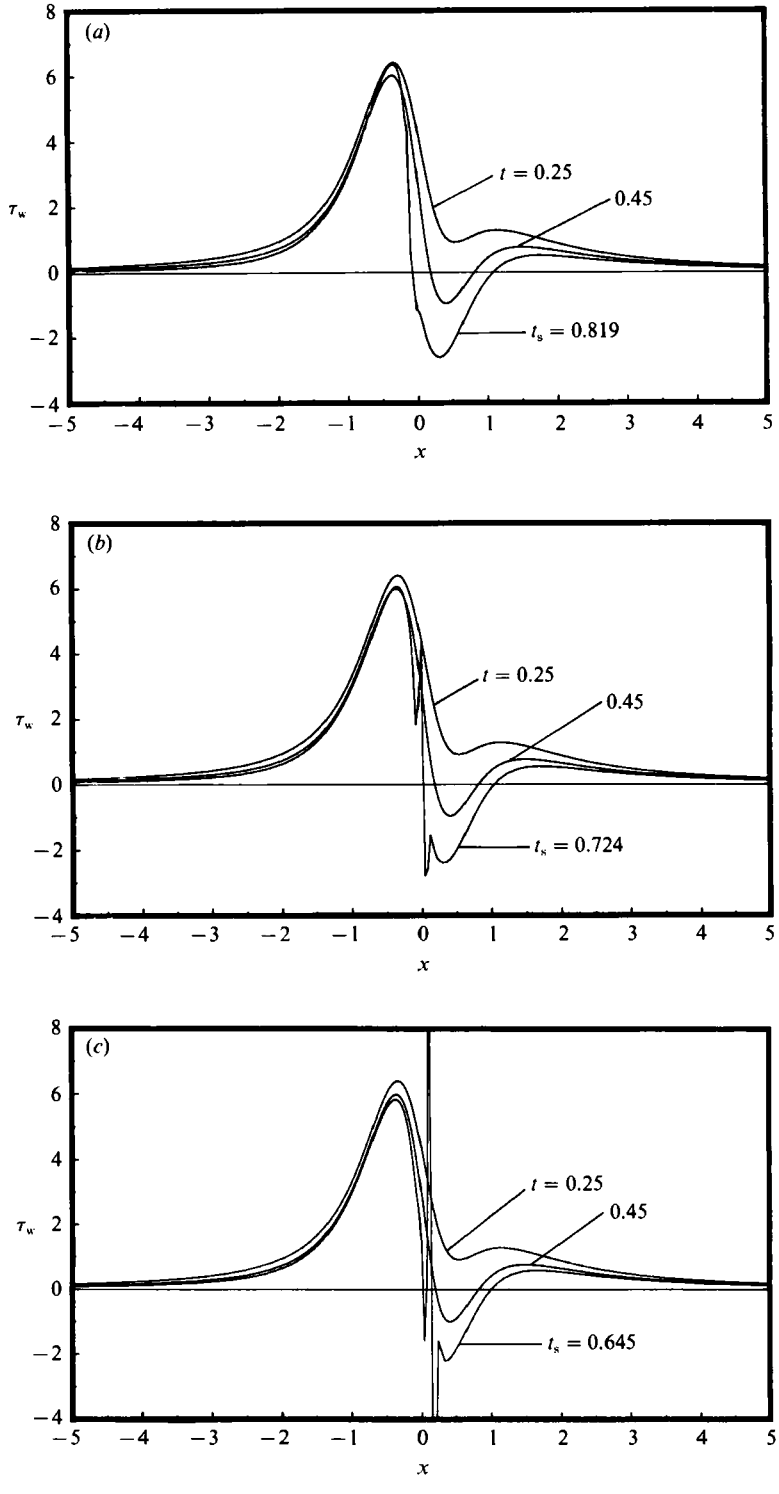

FIGURE 7. Temporal evolution of the wall shear. (a) $Re = 10^7$; (b) $Re = 10^6$; (c) $Re = 10^5$.

Re	t_s	Interval	$\log(c)$	b
10^8	0.897	$[0.819, t_s)$	-0.391 ± 0.065	-0.252 ± 0.016
10^7	0.819	[0.805, 0.816]	-0.778 ± 0.174	-0.253 ± 0.035
10^6	0.724	$[0.680, t_s)$	-0.295 ± 0.092	-0.263 ± 0.022
10^5	0.645	$[0.634, t_s)$	0.892 ± 0.127	-0.234 ± 0.032

TABLE 2. Summary of regression study for temporal behaviour of wall shear near $\hat{x}_s$; $\tau_w = O(t_s - t)^b$; values of t_s for each Re are given in table 1. The theoretical prediction is $b = -0.25$ (Smith 1988*a*).

is shown in figure 7 for $Re = 10^7$, 10^6, 10^5. In all cases the evolution is essentially identical to that associated with the limit problem $Re \to \infty$, except in a narrow streamwise band when interaction is significant as $t \to t_s -$. In figure 7(*a*) the temporal development is shown for $Re = 10^7$, where what appears to be a small distortion is evident near $x_s = -0.091$. For $Re = 10^6$ in figure 7(*b*) and $Re = 10^5$ in figure 7(*c*), the irregularity that develops in the wall shear is clearly evident. The theory of Smith (1988*a*) predicts a singularity in the wall shear as $t \to t_s$, according to (10). As $t \to t_s$ the $\hat{x}$-location corresponding to the minimum gradient (in (95)), $\hat{x}_M$, moves toward $\hat{x}_s$, the location of the singularity. Values of τ_w at $\hat{x}_M$ were recorded over the time intervals indicated in table 2 and a least-squares curve fit to the relation $\tau_w = c(t_s - t)^b$ was carried out to determine c and b. The values of b obtained in this process have a rather small standard error and they support the theoretical prediction of Smith (1988*a*) that $b = -0.25$. Generally, the behaviour of the wall shear at $\hat{x}_M$ was found to be a reasonably reliable criterion for the evaluation of t_s, since τ_w increases monotonically there as $t \to t_s$. The Lagrangian numerical integrations (as in Part 1) can be continued beyond t_s (although the results are not meaningful), since a catastrophic failure of the scheme does not occur at t_s. The onset of erratic behaviour in τ_w was found to be a good indication that the calculation had gone beyond t_s.

7. External flow development as $t \to t_s$

For the limit problem $Re \to \infty$, the mainstream velocity is steady in a frame of reference convecting with the vortex. For the interacting boundary-layer calculations, U_e is unsteady owing to the influence of the boundary layer. However, the only significant deviation from the limit distribution occurred as $t \to t_s$ near $x = x_s$. In figure 8(*a*), U_e is plotted at time t_s for $Re = 10^7$; a slight deviation from the limit distribution may be noted near $x_s = -0.091$. With decreasing Re in figure 8(*b*, *c*), an increasing departure from the limit distribution near x_s may be observed. In figure 8(*c*) there are two spikes in U_e, the larger one being associated with the singularity that develops adjacent to secondary eddy a in figure 6(*a*) and the smaller with tertiary eddy b.

The pressure distribution at $t = t_s$ is shown in figure 9(*a*, *b*) for $Re = 10^7$ and 10^5 respectively. For $Re = 10^7$, a sharp but small distortion occurs near $x_s = -0.091$ in a distribution which is otherwise identical to the steady pressure variation associated with the limit problem $Re \to \infty$. For $Re = 10^8$, the distortion near x_s is barely noticeable when plotted on this same scale (Peridier & Walker 1989). As Re decreases, the local changes in the pressure distribution become sharper but are still concentrated in a very narrow band near where an eruption of the boundary layer is developing. It may be noted in figure 9(*b*), for $Re = 10^5$, that the local changes in

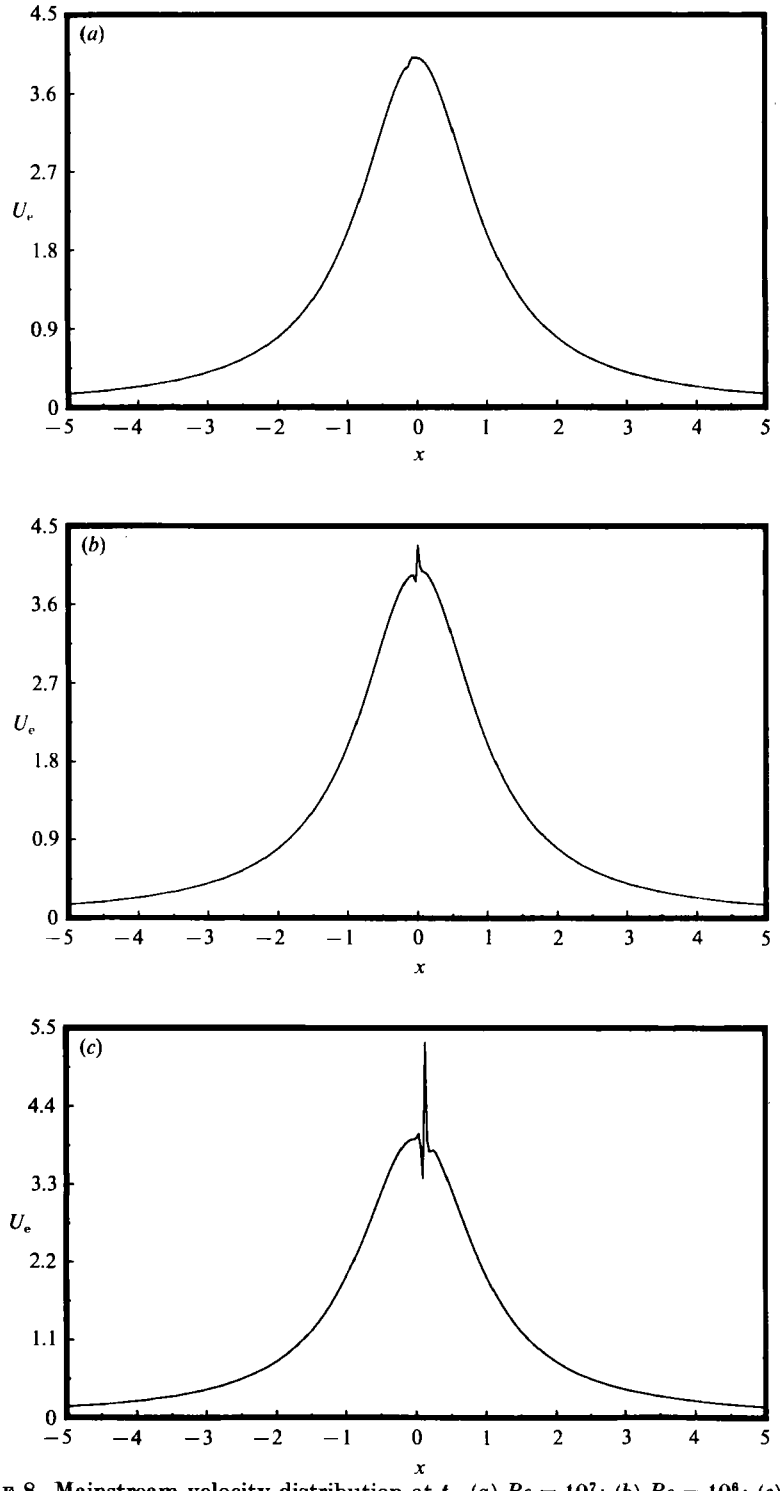

FIGURE 8. Mainstream velocity distribution at t_s. (a) $Re = 10^7$; (b) $Re = 10^6$; (c) $Re = 10^5$.

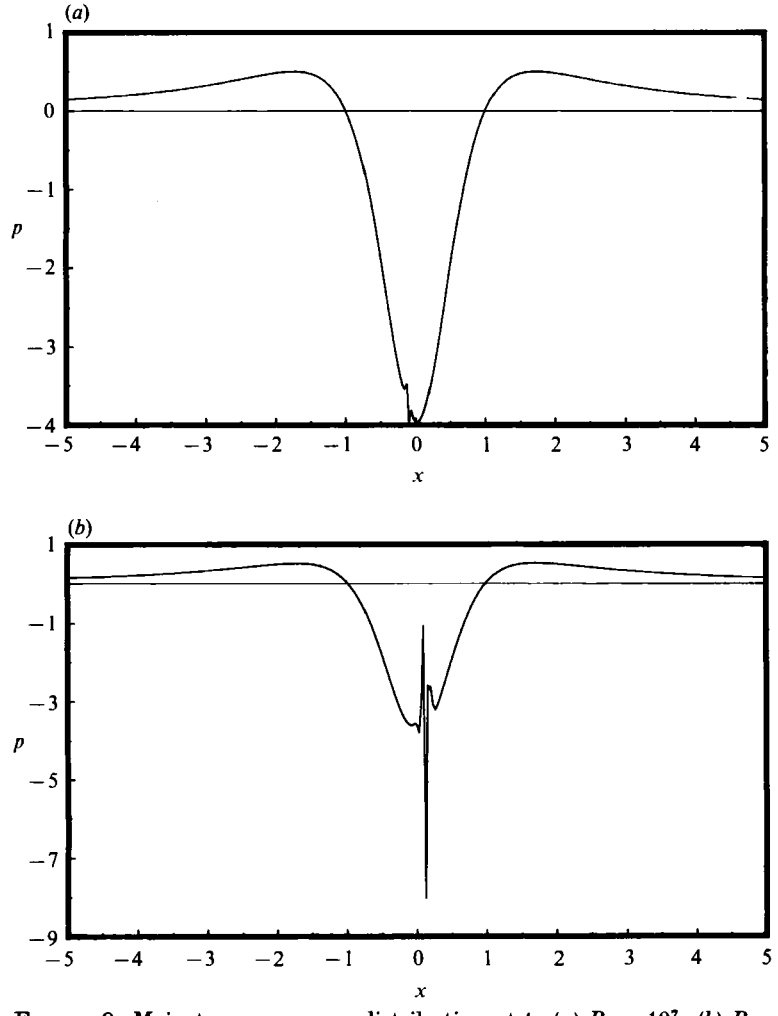

FIGURE 9. Mainstream pressure distribution at t_s. (*a*) $Re = 10^7$; (*b*) $Re = 10^5$.

pressure due to the interaction have magnitudes comparable to the base steady pressure associated with the limit problem. These sharp changes in pressure develop rapidly as interaction evolves as $t \to t_s -$.

The dynamical pressure gradient for the problem is given by

$$-\frac{\partial p}{\partial x} = (U_e - U_v)\frac{\partial U_e}{\partial x} + \frac{\partial U_e}{\partial t}, \tag{97}$$

where U_e is obtained from (74) and $U_v(t)$ is the vortex speed. The pressure gradient at t_s is shown in figure 10(*a*) for $Re = 10^8$ where the departure near $x_s = -0.152$ from the limit distribution, in the form of two spikes, should be noted. With decreasing Re the local behaviour in $\partial p/\partial x$ near x_s becomes more severe as indicated, for example, in figure 10(*b*) for $Re = 10^6$. The analysis of Smith (1988*a*) predicts that $\partial p/\partial x$ is $O((x-x_s)^{-\frac{2}{3}})$ as $t \to t_s$, and while a precise confirmation of this functional behaviour is difficult to establish, the behaviour depicted in figure 10 certainly suggests a singularity. To show the rapid evolution, the pressure gradient at $t_s - 0.015$ and t_s is plotted in figure 11(*a*, *b*), respectively for $Re = 10^5$. Note the change in scale in these

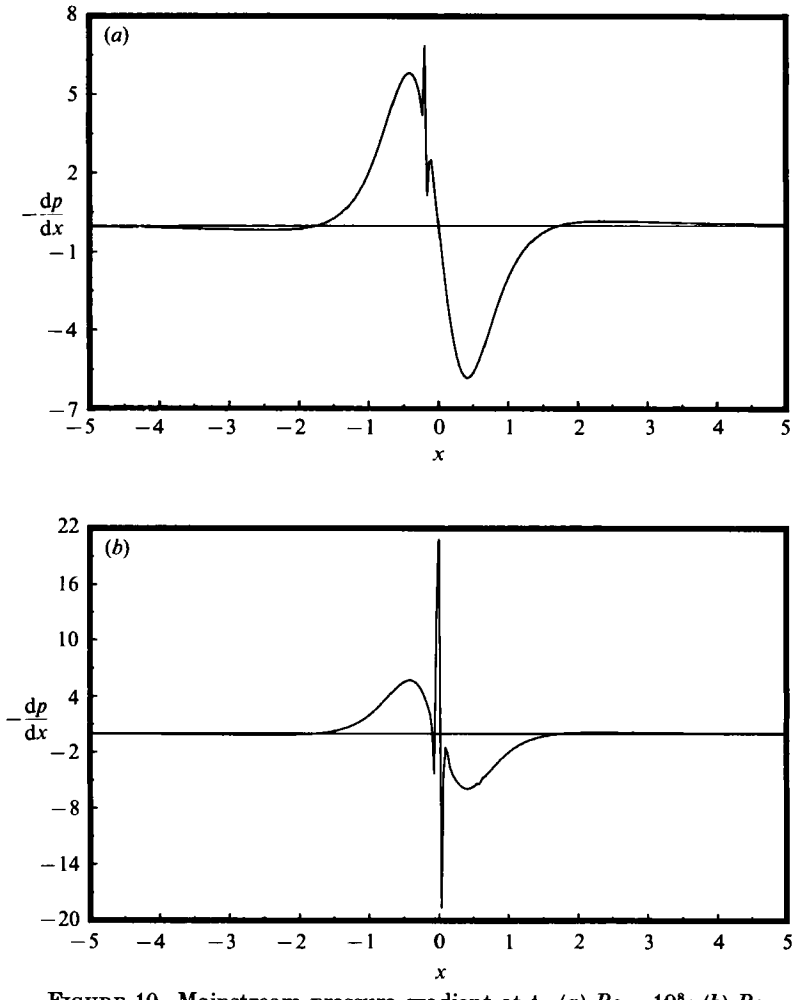

FIGURE 10. Mainstream pressure gradient at t_s. (a) $Re = 10^8$; (b) $Re = 10^6$.

figures and that the local spikes that finally develop in the interaction zone become much larger than the original pressure gradient induced by the vortex.

The predicted behaviour of the maximum pressure gradient and displacement velocity obtained by Smith (1988*a*) is given in (9). A regression analysis was carried out on the present results in a manner similar to that described in connection with table 2, i.e. by tracking the values of these quantities at the point of minimum gradient x_M as $t \to t_s$ and $x_M \to x_s$. Two aspects of the regression analysis should be noted. First the regressions were carried out over time intervals on which the values of $\partial p/\partial x$ and V_d at x_M had a well-defined trend, which is generally in the terminal stages of the calculation near t_s. In some cases, the data became somewhat erratic near t_s and the regression range was terminated slightly in advance of t_s. The intervals used for the regression are shown in tables 2–4. The second point is that V_d and $\partial p/\partial x$ are considerably more difficult than τ_w to evaluate accurately as $t \to t_s$. Nevertheless, tables 3 and 4 summarize the results of regression analysis for relations

$$-\frac{\partial p}{\partial x}\bigg|_{x=x_M} = c(t_s - t)^b, \quad V_d|_{x=x_M} = c(t_s - t)^b. \tag{98}$$

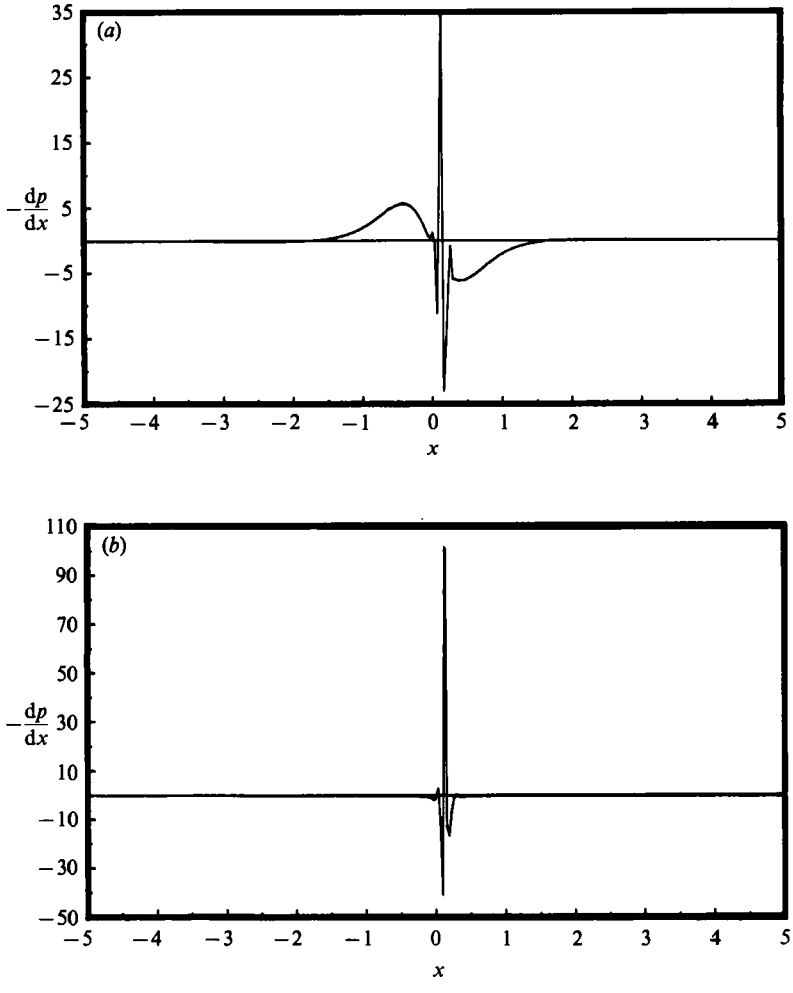

FIGURE 11. Temporal evolution of the mainstream pressure gradient as $t \to t_s$ for $Re = 10^5$. (*a*) $t = t_s - 0.015$; (*b*) $t = t_s$.

Re	t_s	Interval	log (*c*)	*b*
10^8	0.897	[0.855, 0.890]	-1.43 ± 1.03	-0.778 ± 0.28
10^7	0.819	$[0.813, t_s)$	-3.85 ± 0.97	-1.060 ± 0.61
10^6	0.724	$[0.710, t_s)$	-2.39 ± 1.69	-1.110 ± 0.33
10^5	0.645	$[0.623, t_s)$	-17.6 ± 2.90	-4.640 ± 0.70

TABLE 3. Summary of regression study for temporal behaviour of pressure gradient near $x = x_s$; $dp/dx = O(t_s - t)^b$. The predicted theoretical value is $b = -1$ (Smith 1988*a*).

It may be seen from tables 3 and 4 that the present results are in broad agreement with the theory of Smith (1988*a*) which predicts that $b = -1$, with the sole exception being the pressure gradient for $Re = 10^5$. It should be noted, in line with the second point above, that the quantitative evidence here is not as strong as for the wall shear in table 2; the value of $b = -1$ is generally within the 95% confidence intervals in tables 3 and 4, but there is a rather large standard error.

Re	t_s	Interval	$\log(c)$	b
10^8	0.897	[0.855, 0.890]	-2.81 ± 1.07	-1.24 ± 0.31
10^7	0.819	[0.810, t_s)	-1.55 ± 0.53	-0.957 ± 0.094
10^6	0.724	[0.669, t_s)	-0.823 ± 0.97	-1.03 ± 0.18
10^5	0.645	[0.640, t_s)	0.53 ± 1.32	-0.94 ± 0.21

TABLE 4. Summary of regression study for temporal behaviour of v_{max}; $V_d(\tilde{x}_s) = O(t_s - t)^b$. The predicted theoretical value is $b = -1$ (Smith 1988*a*).

8. Comparison with asymptotic theory

The objective of this section is to show that the interacting boundary-layer results are also consistent with the temporal and streamwise scales derived by Elliott *et al.* (1983) for the first interactive stage (cf. figure 1). This is possible here since it is anticipated that the interacting boundary-layer solutions will closely follow the same development as the limit solution ($Re \to \infty$). However, interaction relieves the unsteady separation singularity discussed by Van Dommelen & Shen (1982), Elliott *et al.* (1983), and in Part 1, the IBL solutions then proceed rapidly to the interactive singularity structure of Smith (1988*a*). Nevertheless, the length- and timescales of the first interactive stage should be contained within the IBL results, for large values of Re.

Consider first the timescale associated with the first interactive stage given in (1). As discussed in §1, numerical solutions of the interactive problem given in (3)–(5) have not yet been obtained; however, a singularity is expected to develop at finite time and let t_{Is} and X_{Is} denote the scaled time and streamwise position (cf. (1)) at which this breakdown occurs. It is believed that the quantity t_{Is} is related to the breakdown times in the interactive problem by

$$t_{Is} = Re^{\frac{2}{11}}(t_s(Re) - t_s(\infty)), \tag{99}$$

where $t_s(Re)$ is the breakdown time at a finite value of Re and $t_s(\infty)$ is the corresponding value for the limit problem. A regression analysis of the data in table 1 was carried out for a relation of the form

$$\log(t_s(\infty) - t_s(Re)) = a + b\log Re, \tag{100}$$

and the estimated values of a and b are

$$a = 1.21\pm0.36, \quad b = -0.190\pm0.24, \tag{101}$$

where the errors represent 95% confidence intervals. Since $\frac{2}{11} = 0.182$, the estimate of b is in good agreement with the scale predicted by Elliott *et al.* (1983).

Next consider the streamwise scale of the eruptive zone which is predicted to be $O(Re^{-\frac{3}{11}})$ by Elliott *et al.* (1983). The values of the breakdown locations $x_s(\infty)$ and $x_s(Re)$ given in table 1 represent distances from the origin in a reference frame moving with the vortex. In order to make a comparison, it is necessary to express these distances in a common frame. To this end consider a laboratory reference frame whose origin corresponds to the instantaneous location of the vortex for the limit problem at $t_s(\infty)$; for the cases at finite Re, the vortex is assumed to pass the same location at $t_s(Re)$. In the laboratory frame, the velocity of the singularity is

$$U_e(x_s(Re)) = U_v - K(Re). \tag{102}$$

The vortex velocity $U_v = 1 + O(Re^{-\frac{1}{2}})$ and was found to be close to 1 during the course

of the integrations, with the maximum deviation being on the order of 1.004 for $Re = 10^4$ at $t = t_s$. Taking $U_v = 1$, the analysis of Elliott *et al.* (1983) suggests

$$x_s(Re) - x_s(\infty) + U_{e_s} U_s(t_s(\infty) - t_s(Re)) = O(Re^{-\frac{3}{11}}). \tag{103}$$

A regression analysis on the relation

$$\log(x_s(Re) - x_s(\infty) - \{K(Re) - 1\}\{t_s(\infty) - t_s(Re)\}) = e + f \log Re, \tag{104}$$

using the values listed in table 1 produced the following results:

$$e = 3.05 \pm 0.23, \quad f = -0.295 \pm 0.015. \tag{105}$$

Since $\frac{3}{11} = 0.273$, the value of f is in agreement with the scale predicted by Elliott *et al.* (1983).

9. Conclusions

The interacting boundary-layer results obtained here show fairly firmly that a singularity develops in the interactive formulation at finite time. Consequently, the utility of conventional interacting boundary-layer methods is believed to be limited to computing unsteady separation up to the onset of interaction with the external flow and no further. This conclusion is in agreement with the recent theory of Smith (1988*a*) but is apparently at variance with three recent computational studies (Henkes & Veldman 1987; Cebeci *et al.*1988; and Riley & Vasantha 1989) which suggest that conventional IBL methods may relax the singularity which is known to occur in the limit problem. The apparent discrepancy may be due in part to the use of first-order schemes in the cited studies for evaluating the Cauchy integral in the interaction condition. In a fourth computational study, Chuang & Conlisk (1989) used a second-order method for the Cauchy integral and eventually encountered a severe instability in the IBL computations which they attributed to a possible singularity. A further difficulty with the aforementioned IBL studies is that they were carried out using a conventional Eulerian formulation for the boundary-layer problem. Such methods usually are not able to properly resolve the flow field as an eruption starts to develop, because the streamwise extent of the erupting zone narrows progressively and ultimately reaches a stage wherein adequate resolution using a fixed mesh in space in the Eulerian frame is impossible. In principle, some type of time-dependent adaptive mesh algorithm (see, for example, Riley & Vasantha 1989) may permit accurate evaluation of such eruptive flows in the Eulerian formulation. The Lagrangian formulation seems the best currently available method to accurately track the erupting flow toward an interaction.

The present results confirm the Reynolds-number dependence of the streamwise length- and timescales described in the analysis of Elliott *et al.* (1983) for the first interactive stage. The effects of interaction relieve the separation singularity (Van Dommelen 1981) but only for a brief period of time. The present results also show that the solution evolves toward the interactive singularity structure described by Smith (1988*a*), in which the wall shear, pressure gradient, and normal velocity become singular at a streamwise location x_s as $t \to t_s$. The present results appear to closely confirm the asymptotic theory. Velocity profiles near x_s are shown in figure 12 for $Re = 10^5$ and are suggestive of the three-tier structure described by Smith (1988*a*) and sketched in figure 2. It may be noted that in contrast to the terminal structure of the limit problem (Part 1) where the profiles are very flat near x_s as $t \to t_s(\infty)$, the profiles in figure 12 depict a rotational flow near x_s. We observe, as an

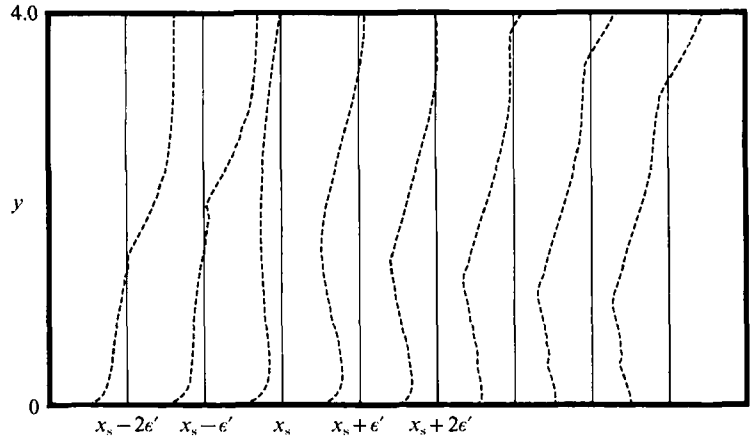

FIGURE 12. Velocity profiles near x_s at $t = t_s$ for $Re = 10^5$; $\epsilon' = 0.0045$.

aside, that in general terms the present work tends to support the view that break-up can occur in any unsteady interacting boundary-layer formulation at finite time (Smith 1988*a*); subsequent theoretical and computational studies in progress are adding further support. There is also an analogous situation regarding break-up in steady interactive separation (Smith 1988*b*; Smith & Khorrami 1991).

The present interacting calculations show that the effect of interaction is to promote and hasten the breakdown of the boundary-layer solution rather than delay or mitigate a singularity. The breakdown time for finite Reynolds numbers $t_s(Re)$ is always less than that for the limit problem $t_s(\infty)$ and decreases with decreasing Reynolds number. As Re decreases, the surface flow, in a sense, appears to evolve toward a more mature state just prior to breakdown and to develop complex effects near the surface including: (i) bifurcation of the secondary eddy into several substructures and (ii) the evolution of a tertiary eddy which has often been observed in experiments. The pressure response to the onset of interaction has been shown in figures 9 and 10, and it may be noted that such responses will be extremely difficult to resolve with current surface pressure measurement techniques. The type of eruptions discussed in this study are of interest relating to fully turbulent flows (Walker *et al.* 1989; Walker 1990*a*, *b*; Smith *et al.* 1990, 1991) and flows undergoing transition to turbulence. The main difficulty with measuring a pressure response of the type shown in figures 9 and 10 is that it develops very abruptly in time, as well as having a complex structure in a narrow streamwise band.

Finally, it is of interest to inquire how the interactive singularity of Smith (1988*a*) can be relieved so that a practical calculation scheme can be structured to proceed further in time into the strong interaction. It seems likely that it is necessary to incorporate the influence of the pressure gradient normal to the surface, at least in a narrow zone bracketing the eruptive region; this aspect is currently under consideration (Hoyle, Smith & Walker 1991; Hoyle 1991) with three-dimensional effects also being considered.

The authors would like to thank AFOSR for support of this work under Grants AFOSR 89-0065 and AFOSR-89-0475 as well as NATO for a travel grant (86/197). The referees' comments are also gratefully acknowledged.

Appendix

Here the coefficients associated with the second-order method for the evaluation of the Cauchy integral (72) are given. First consider the main portion given by (76) and (78), for which the numerical algorithm is of the form (85). It is evident from (78), (81) and (82) that

$$\alpha_{ij} = \Delta\hat{x} \int_{-\frac{1}{2}}^{\frac{1}{2}} \frac{\mathrm{d}\mu}{\sin(r_{ij} - \pi\epsilon\mu)}, \tag{A 1}$$

$$\beta_{ij} = (\Delta\hat{x})^2 \int_{-\frac{1}{2}}^{\frac{1}{2}} \frac{\mu\,\mathrm{d}\mu}{\sin(r_{ij} - \pi\epsilon\mu)}, \tag{A 2}$$

where $\epsilon = \frac{1}{2}\Delta\hat{x}$ and

$$r_{ij} = \tfrac{1}{2}\pi(\hat{x}_i - \hat{x}_j) = (i-j)\,\epsilon\pi. \tag{A 3}$$

The integral (A 1) may be evaluated in closed form, namely

$$\alpha_{ij} = \frac{1}{\pi}\log\left\{\frac{\sin r_{ij} + \sin(\frac{1}{2}\pi\epsilon)}{\sin r_{ij} - \sin(\frac{1}{2}\pi\epsilon)}\right\}^2. \tag{A 4}$$

To calculate an approximation to the integral in (A 2), first note that

$$\sin(r_{ij} - \pi\epsilon\mu) = \sin r_{ij} - \pi\epsilon\mu\cos r_{ij} + O(\epsilon^2), \tag{A 5}$$

for small ϵ. Upon substitution in (A 2), the following approximate expression for β_{ij} is obtained:

$$\beta_{ij} = -\frac{(\Delta\hat{x})^2}{\pi\epsilon\cos r_{ij}}\left\{1 + \frac{\tan r_{ij}}{\pi\epsilon}\log\left|\frac{2\sin r_{ij} - \pi\epsilon\cos r_{ij}}{2\sin r_{ij} + \pi\epsilon\cos r_{ij}}\right|\right\}. \tag{A 6}$$

For r_{ij} of $O(1)$, equation (A 6) has the asymptotic form

$$\beta_{ij} \sim \tfrac{1}{3}\pi\epsilon^3 \frac{\cot r_{ij}}{\sin r_{ij}} + \ldots, \tag{A 7}$$

which may be used to evaluate β_{ij} efficiently for r_{ij} larger than about $\frac{1}{4}\pi$. Note that both α_{ij} and β_{ij} decrease with increasing r_{ij} but that the rate of decrease in β_{ij} is much more dramatic.

Next consider the evaluation of the tails of the Cauchy integral defined in (77) when the asymptotic expansion of F is known for large $|x|$ (cf. (87)). For terms in F which are $O(x^{-k})$, it is evident from (77) that the evaluation of integrals

$$a_k(x_i) = \frac{1}{\pi x_i^k}\int_{R/x_i}^{\infty} \frac{\mathrm{d}\tau}{\tau^k(1-\tau)}, \quad b_k(x_i) = \frac{1}{\pi x_i^k} = \int_{-\infty}^{-R/x_i} \frac{\mathrm{d}\tau}{\tau^k(1-\tau)} \tag{A 8}$$

for $x_i \neq 0$, is required and

$$a_k(0) = -\frac{1}{\pi}\int_R^{\infty} \frac{\mathrm{d}s}{s^{k+1}}, \quad b_k(0) = -\frac{1}{\pi}\int_{-\infty}^{-R} \frac{\mathrm{d}s}{s^{k+1}} \tag{A 9}$$

for $x_i = 0$. In the present application, the required integrals are

$$a_3(x_i) = \frac{1}{2\pi x_i^3}\{\gamma(2+\gamma) + \log(\gamma-1)^2\}, \tag{A 10}$$

$$b_3(x_i) = \frac{1}{2\pi x_i^3}\{\gamma(2-\gamma) - \log(\gamma+1)^2\} \tag{A 11}$$

for $x_i \neq 0$, where $\gamma = x_i/R$. For $x_i = 0$

$$a_3(0) = b_3(0) = -1/(3\pi R^3). \tag{A 12}$$

In addition,

$$a_5(x_i) = \frac{1}{2\pi x_i^5}\{\gamma(2+\gamma(1+\gamma)(\tfrac{2}{3}+\tfrac{1}{2}\gamma)) + \log(\gamma-1)^2\}, \tag{A 13}$$

$$b_5(x_i) = \frac{1}{2\pi x_i^5}\{\gamma(2-\gamma(1-\gamma)(\tfrac{2}{3}-\tfrac{1}{2}\gamma)) - \log(\gamma+1)^2\} \tag{A 14}$$

for $x_i \neq 0$ and

$$a_5(0) = b_5 = -1/(5\pi R^5). \tag{A 15}$$

Note that from the definition of R in (79)

$$|\gamma| = |x_i/R| < 1 \quad \text{for all} \quad i. \tag{A 16}$$

REFERENCES

Abramowitz, M. & Stegun, I. A. 1964 *Handbook of Mathematical Functions*. US Government Printing Office, Washington, DC.

Acarlar, M. S. & Smith, C. R. 1987*a* A study of hairpin vortices in a laminar boundary layer. Part 1. Hairpin vortices generated by a hemisphere protuberance. *J. Fluid Mech.* **175**, 1–41.

Acarlar, M. S. & Smith, C. R. 1987*b* A study of hairpin vortices in a laminar boundary layer. Part 2. Hairpin vortices generated by fluid injection. *J. Fluid Mech.* **175**, 43–83.

Brotherton-Ratcliffe, R. V. & Smith, F. T. 1987 Complete breakdown of an unsteady interacting boundary layer (over a surface distortion or in a liquid layer). *Mathematika* **34**, 86–100.

Brown, S. N., Cheng, H. K. & Smith, F. T. 1988 Nonlinear instability and break-up of separated flow. *J. Fluid Mech.* **193**, 191–216.

Cebeci, T., Khattab, A. A. & Schimke, S. M. 1988 Separation and reattachment near the leading edge of a thin oscillating airfoil. *J. Fluid Mech.* **188**, 253–274.

Chu, C. C. & Falco, R. E. 1988 Vortex ring/viscous wall layer interaction model of the turbulence production process near walls. *Exp. Fluids* **6**, 305.

Chuang, F. S. & Conlisk, A. T. 1989 Effect of interaction on the boundary layer induced by a convected rectilinear vortex. *J. Fluid Mech.* **200**, 337–365.

Conlisk, A. T. 1989 The pressure field in intense vortex–boundary layer interaction. *27th Aerospace Sciences Meeting, Reno, NV, AIAA Paper* 89-0293.

Cowley, S. J., Van Dommelen, L. L. & Lam, S. T. 1990 On the use of Lagrangian variables in the description of unsteady boundary-layer separation. *Phil. Trans. R. Soc. Lond.* A **333**, 343–378.

Doligalski, T. L. & Walker, J. D. A. 1984 The boundary layer induced by a convected two-dimensional vortex. *J. Fluid Mech.* **139**, 1–28.

Ece, M. C., Walker, J. D. A. & Doligalski, T. L. 1984 The boundary layer on an impulsively started rotating and translating cylinder. *Phys. Fluids* **23**, 1077–1089.

Elliott, J. W., Cowley, S. J. & Smith, F. T. 1983 Breakdown of boundary layers: (i) on moving surfaces; (ii) in self-similar unsteady flow; (iii) in fully unsteady flow. *Geophys. Astrophys. Fluid Dyn.* **25**, 77–138.

Ersoy, S. & Walker, J. D. A. 1985 Viscous flow induced by counterrotating vortices. *Phys. Fluids* **28**, 2687–2698.

Ersoy, S. & Walker, J. D. A. 1986 Flow induced at a wall by a vortex pair. *AIAA J.* **24**, 1597–1605.

Goldstein, S. 1948 On laminar boundary-layer flow near a point of separation. *Q. J. Mech. Appl. Maths* **1**, 43–69.

Harvey, J. K. & Perry, F. J. 1971 Flowfield produced by trailing vortices in the vicinity of the ground. *AIAA J.* **9**, 1659–1660.

Head, M. R. & Bandyopadhyay, P. 1981 New aspects of turbulent boundary layer structure. *J. Fluid Mech.* **107**, 297–338.

Henkes, R. A. W. M. & Veldman, A. E. P. 1987 On the breakdown of the steady and unsteady interacting boundary-layer description. *J. Fluid Mech.* **179**, 513–529.

HOYLE, J. M. 1991 Ph.D. thesis, University of London, in preparation.

HOYLE, J. M., SMITH, F. T. & WALKER, J. D. A. 1991 On sublayer eruption and vortex formation. *Comput. Phys. Commun.* **65**, 151–157.

LOU, T.-W. 1990 Interactive boundary-layer solutions for vortex-induced separation. M.Sc. thesis, Lehigh University.

NAPOLITANO, M., WERLE, M. J. & DAVIS, R. T. 1978 Numerical solution of the triple-deck equations for supersonic and subsonic flow past a hump. *David Taylor Naval Shipyard Research and Development Center Rep.* AFL78-6-42.

PERIDIER, V., SMITH, F. T. & WALKER, J. D. A. 1991 Vortex-induced boundary-layer separation. Part 1. The limit problem $Re \rightarrow \infty$. *J. Fluid Mech.* **232**, 99–131.

PERIDIER, V. J. & WALKER, J. D. A. 1988 An algorithm for unsteady flows with strong convection. *NASA Tech. Mem.* 100828; ICOMP-88-5. NASA Lewis Research Center.

PERIDIER, V. J. & WALKER, J. D. A. 1989 Vortex induced boundary layer separation. *AFOSR Rep.* FM-13. Department of Mechanical Engineering and Mechanics, Lehigh University; AFOSR-TR-90-0458 (also available AD-221564).

PERRY, A. E. & CHONG, M. S. 1982 On the mechanisms of wall turbulence. *J. Fluid Mech.* **119**, 173–217.

RILEY, N. & VASANTHA, R. 1989 Unsteady high Reynolds number flows. *J. Fluid Mech.* **205**, 243–262.

SEARS, W. R. & TELIONIS, D. P. 1971 Unsteady boundary-layer separation. In *Recent Research on Unsteady Boundary Layers*, pp. 404–447. Laval University Press, Quebec.

SEARS, W. R. & TELIONIS, D. P. 1975 Boundary-layer separation in unsteady flow. *SIAM J. Appl. Maths* **28**, 215–235.

SMITH, F. T. 1982 On the high Reynolds number theory of laminar flows. *IMA J. Appl. Maths* **28**, 207–281.

SMITH, F. T. 1988*a* Finite-time breakup can occur in any unsteady interacting boundary layer. *Mathematica* **35**, 256–273.

SMITH, F. T. 1988*b* A reversed-flow singularity in interacting boundary layers. *Proc. R. Soc. Lond.* A **420**, 21–52.

SMITH, F. T. & KHORRAMI, A. F. 1991 The interactive breakdown in supersonic ramp flow. *J. Fluid Mech.* **224**, 197–215.

SMITH, C. R., WALKER, J. D. A., HAIDARI, A. H. & SOBRUN, U. 1991 On the dynamics of near-wall turbulence. *Phil. Trans. R. Soc. Lond.* A (in press).

SMITH, C. R., WALKER, J. D. A., HAIDARI, A. H. & TAYLOR, B. K. 1990 Hairpin vortices in turbulent boundary layers: the implications for reducing surface drag. In *Structure of Turbulence and Drag Reduction* (ed. A. Gyr), pp. 51–58. Springer.

STEWARTSON, K. 1974 Multistructured boundary layers on flat plates and related bodies. *Adv. Appl. Mech.* **14**, 145–239.

VAN DOMMELEN, L. L. 1981 Unsteady boundary-layer separation. Ph.D. dissertation, Cornell University.

VAN DOMMELEN, L. L. & SHEN, S. F. 1980 The spontaneous generation of the singularity in a separating boundary layer. *J. Comput. Phys.* **38**, 125–140.

VAN DOMMELEN, L. L. & SHEN, S. F. 1982 The genesis of separation. In *Proc. Symp. on Numerical and Physical Aspects of Aerodynamic Flow, Long Beach, California* (ed. T. Cebeci), pp. 283–311. Springer.

WALKER, J. D. A. 1978 The boundary layer due to a rectilinear vortex. *Proc. R. Soc. Lond.* A **359**, 167–188.

WALKER, J. D. A. 1990*a* Wall-layer eruptions in turbulent flows. In *Structure of Turbulence and Drag Reduction* (ed. A. Gyr), pp. 109–110. Springer.

WALKER, J. D. A. 1990*b* Models based on dynamical features of the wall layer. *Appl. Mech. Rev.* **43**, S232–S239.

WALKER, J. D. A., ABBOTT, D. E., SCHARNHORST, R. K. & WEIGAND, G. G. 1989 Wall-layer model for velocity profile in turbulent flows. *AIAA J.* **27**, 140–149.

WALKER, J. D. A., SMITH, C. R., DOLIGALSKI, T. L. & CERRA, A. W. 1987 Impact of a vortex ring of a wall. *J. Fluid Mech.* **181**, 99–140.